Remote Sensing of Environment 280 (2022) 113208

Contents lists available at ScienceDirect

Remote Sensing of Environment

journal homepage: www.elsevier.com/locate/rse

Sentinel-1 interferometric coherence as a vegetation index for agriculture

Arturo Villarroya-Carpio [a], Juan M. Lopez-Sanchez [a,*], Marcus E. Engdahl [b]

[a] Institute for Computer Research, University of Alicante, Alicante, Spain
[b] European Space Research Institute, European Space Agency, Frascati, Italy

ARTICLE INFO

Edited by Jing M. Chen

Keywords:
Agriculture
Sentinel-1
Synthetic aperture radar (SAR)
Interferometry
Coherence
Vegetation index
NDVI

ABSTRACT

In this study, the use of Sentinel-1 interferometric coherence data as a tool for crop monitoring has been explored. For this purpose, time series of images acquired by Sentinel-1 and 2 spanning 2017 have been analysed. The study site is an agricultural area in Sevilla, Spain, where 16 different crop species were cultivated during that year. The time series of 6-day repeat-pass coherence measured at each polarimetric channel (VV and VH), as well as their difference, have been compared to the NDVI and to the backscattering ratio (VH/VV) and other indices based on backscatter. The contribution of different decorrelation sources and the effect of the bias from the space-averaged sample coherence magnitude estimation have been evaluated. Likewise, the usage of 12 days as temporal baseline was tested. The study has been carried for three different orbits, characterised by different incidence angles and acquisition times. All results support using coherence as a measure for monitoring the crop growing season, as it shows good correlations with the NDVI ($R^2 > 0.7$), and its temporal evolution fits well the main phenological stages of the crops. Although each crop shows its own evolution, the performance of coherence as a vegetation index is high for most of them. VV is generally more correlated with the NDVI than VH. For crop types characterised by low plant density, this difference decreases, with VH even showing higher correlation values in some cases. For a few crop types, such as rice, the backscattering ratio outperforms the coherence in following the growth stages of the plants. Since both coherence and backscattering are directly computed from the radar images, they could be used as complementary sources of information for this purpose. Notably, the measured coherence performs well without the need of compensating the thermal noise decorrelation or the bias due to the finite equivalent number of looks.

1. Introduction

Data acquired by synthetic aperture radar (SAR) sensors mounted on board of Earth Observation satellites have proven their potential in agricultural crop monitoring (Steele-Dunne et al., 2017; Mandal et al., 2021), especially thanks to the consistent acquisition schedule they provide, not affected by clouds and day/night time. Radar measurements are sensitive to structural and dielectric characteristics of the scene (vegetation and soil), hence providing an excellent complement to the most widely used monitoring schemes based on optical data.

In optical remote sensing of crops, vegetation indices (VI) are usually exploited to better match the data with the targeted features in the scene, as they provide physically interpretable descriptors of vegetation covers and are correlated with biophysical variables of interest, such as leaf area index (LAI). Optical VIs are defined as combinations of values measured at different spectral bands, being NDVI (Normalised Difference VI) the most widely used (Bannari et al., 1995; Haboudane et al., 2004). Equivalently, there exists a set of vegetation indices defined on the basis of radar data, which are also sensitive to crop biophysical variables. SAR vegetation indices are mostly based on either the backscattered intensity at different polarimetric channels, e.g. by using ratios (Kim and van Zyl, 2009), or on descriptors extracted from polarimetry, e.g. polarisation signatures, outputs of decompositions, etc. A recent review of radar vegetation indices can be consulted in (Mandal et al., 2021). The use of radar VIs is constrained by the available polarimetric channels, which depend on the sensor. Consequently, there are indices defined for dual-, compact-, and quad-polarimetric data (Mandal et al., 2020a,b).

Besides the observables derived from measured backscattered intensity (backscattering coefficients and polarimetric descriptors), radar satellites also provide access to interferometric data. In SAR interferometry (InSAR), pairs of images are combined to produce phase measurements related to the scene vertical dimension and other scene properties (Bamler and Hartl, 1998). A key interferometric observable is the interferometric coherence, which is employed as a direct measure

* Corresponding author.
E-mail address: juanma.lopez@ua.es (J.M. Lopez-Sanchez).

https://doi.org/10.1016/j.rse.2022.113208
Received 20 April 2022; Received in revised form 18 July 2022; Accepted 30 July 2022
Available online 16 August 2022

on the quality of the associated interferometric phase, and hence of the derived products. There exist diverse factors that influence the interferometric coherence (Zebker and Villasenor, 1992), whose relative importance depend on scene characteristics, on sensor features, and on the interferometric configuration. Therefore, coherence is by itself a valuable measurement with sensitivity to the properties of the crop in the scene, as it will be exploited in this work.

When the two images are acquired at different times, repeat-pass InSAR (Rosen et al., 2000) is useful to detect changes in the scene since they cause a decrease in interferometric coherence. This loss of coherence is usually denoted as *temporal decorrelation* and is the primary cause of coherence loss over agricultural crops due to the fast growth of plants and the wind-induced movement of vegetation elements. In a broader context, repeat-pass interferometry was tested in the past for land cover mapping by using time series of ERS tandem data (Strozzi et al., 2000; Engdahl and Hyyppä, 2003), with 1-day revisit time, and more recently with Sentinel-1 data (Sica et al., 2019; Jacob et al., 2020), with 6-day revisit time. For the specific application of crop-type mapping, temporal decorrelation is present in areas with vegetation, whereas bare surfaces usually keep a high coherence over longer periods. Therefore, since presence or absence of vegetation provides information related to the crop calendar, which normally depends on the crop type, time series of repeat-pass coherence have proven very useful in crop classification (Busquier et al., 2020; Mestre-Quereda et al., 2020; Nikaein et al., 2021).

Besides its use in crop-type mapping, repeat-pass coherence was also evaluated for the estimation of agricultural crop parameters by Wegmuller and Werner (1997), Engdahl et al. (2001), and Blaes and Defourny (2003). In these experiments, ERS images with 1 day of separation were combined in interferometric pairs, and coherence was found sensitive to crop height and canopy cover. The physical interpretation provided is based on the high coherence expected from the soil and the temporal decorrelation produced by the vegetation layer. The combination of both effects, which depends on crop height and canopy cover, reflects the crop growth. Unfortunately, the lack of availability of SAR images acquired with short revisit times disabled further studies in this direction for a long time. Alternatively, single-pass interferograms computed with pairs of images acquired by the TanDEM-X system, formed by two nearly identical satellites flying in a close formation, have been also used for crop height retrieval more recently (Erten et al., 2016; Lopez-Sanchez et al., 2017; Lee et al., 2018; Romero-Puig and Lopez-Sanchez, 2021). In that case, in absence of temporal decorrelation, the sensitivity of coherence to crop height is based on volume decorrelation, for which a very large baseline (distance between the satellites orbits) is required.

With the launch of the Sentinel-1 constellation (S1), which provides a revisit period of 6 days over Europe and 12 days elsewhere, the interest in exploring the potential of repeat-pass interferometry in crop monitoring has grown again. In fact, the analysis of the time series of 6-day S1 coherence employed by Mestre-Quereda et al. (2020) revealed obvious temporal patterns which could be easily associated with the growth of plants for many of the crops present in the test site, as well as clear differences between the VV and VH channels. The present work stems from those time series and is firstly intended to provide an in-depth analysis of them as a function of crop growth.

Recently, the relationship between S1 interferometric coherence and crop growth has been also explored to some extent by other authors. Nasirzadehdizaji et al. (2021) analysed time series of coherence and intensity values by comparing them with the growth condition of three different crops: maize, sunflower, and wheat. Coherence was useful to estimate the main growth stage of these crops (using a 3-stage scale: sowing, growth, harvest), and the authors also studied the difference between VV and VH. Similarly, Pandit et al. (2022) studied the identification of phenological stages of two crops, i.e. bengal-gram and tomato, using time series of 12-day S1 coherence in an Indian test site. In this case, only the VV channel was inspected, and its evolution was qualitatively interpreted with the help of NDVI time series obtained from Sentinel-2 (S2) data.

The present work is aimed at extending previous works on the use of repeat-pass S1 coherence for agriculture monitoring. With this goal, the number of crop types studied has been increased up to 16, and fallow has been also analysed. More importantly, both the coherences at VV and VH, as well as their difference, have been exploited in a quantitative analysis by comparing them with the NDVI and with other radar VIs. In addition, the relative importance of the main sources of decorrelation which provide sensitivity (temporal decorrelation and thermal noise decorrelation) has been studied, and the bias induced by the finite number of samples (especially for very low coherences) has been taken into account.

Table 1
Number of fields and total area occupied by each crop.

Crop type	Fields	Total area (km^2)
Alfalfa	84	4.10
Carrot	74	2.22
Chickpea	26	0.55
Cotton	1369	60.47
Fallow	728	1.17
Maize	173	6.73
Onion	62	1.58
Pepper	33	0.67
Potato	21	0.43
Pumpkin	27	0.96
Quinoa	34	1.08
Rice	300	27.81
Sugar beet	554	21.23
Sunflower	145	6.31
Sweet potato	44	1.27
Tomato	829	32.46
Wheat	107	4.38
TOTAL	4610	173.43

2. Materials and methods

2.1. Test site and data sets

The test site is an agricultural area, named BXII Sector, located in Sevilla, Spain, centered at 37 N 6.1 W. In this zone, 16 different crop species were cultivated in 2017, and some fields were left as fallow, which hence constitutes an additional land cover class. The reference data and the satellite imagery (S1 and S2 data) employed in this study are described in this section.

2.1.1. Reference data

The crop types cultivated at each one of the parcels of the test site are identified in the official land parcel identification system of 2017, see Fig. 1 and Table 1. This dataset has already been used in previous works (Mestre-Quereda et al., 2020; Di Martino et al., 2022).

In order to provide visual information about the characteristics of every crop type, photographs are shown in Fig. 2. It is important to note how each crop reaches a certain level of ground coverage. Being aware of this can be helpful to know whether there is a significant component of the signal received coming from the soil and not from the vegetation, which will be useful for the physical interpretation of the SAR measurements. For rice, the ground is flooded before sowing and is kept flooded for the whole cultivation period.

An approximate calendar for all crop types in this geographical region is available (Fig. 3). The exact dates of sowing and harvest vary depending on plots and farmers, showing differences of up to 1–3 months in some cases. For certain crops, the harvesting of the first planted fields in the season overlaps with the sowing of the last fields, therefore no intermediate growth period is shown in this calendar. Alfalfa is a particular case, since the crop is not fully harvested at once, but periodically cut and left to resprout, thus having a longer cycle. In addition, daily rainfall and wind speed data have been obtained from the *Sistema de Información Agroclimática para el Regado* (SIAR, 2022).

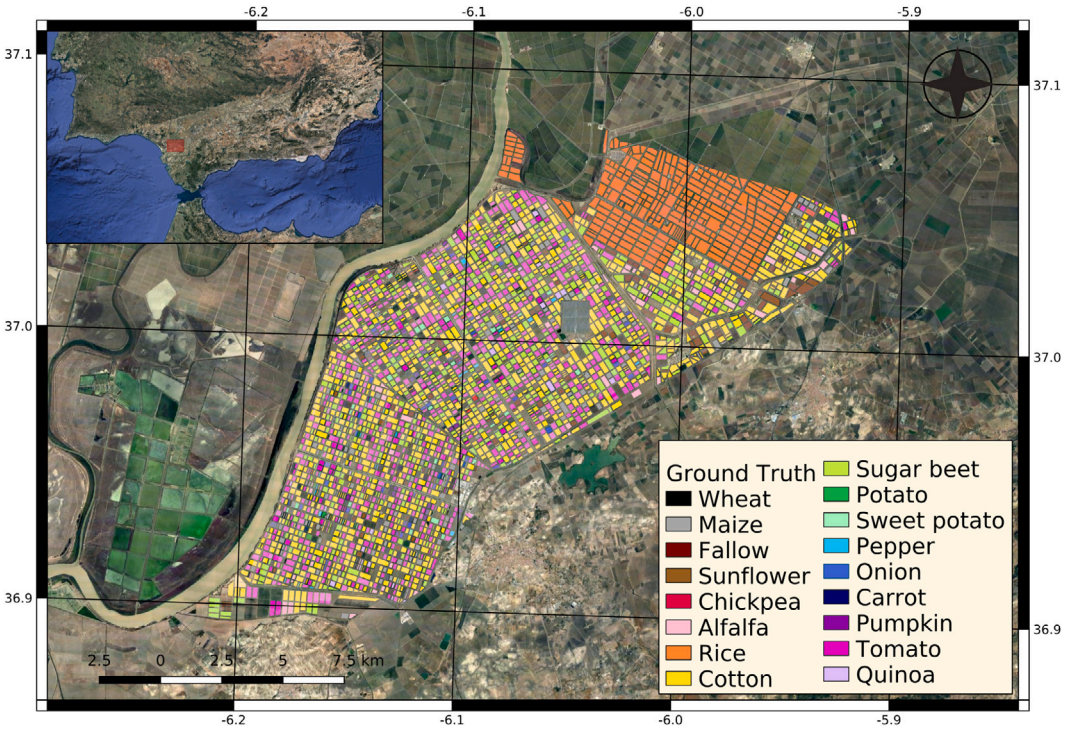

Fig. 1. Map of the test site in Sevilla, with the reference data indicating all crop types.

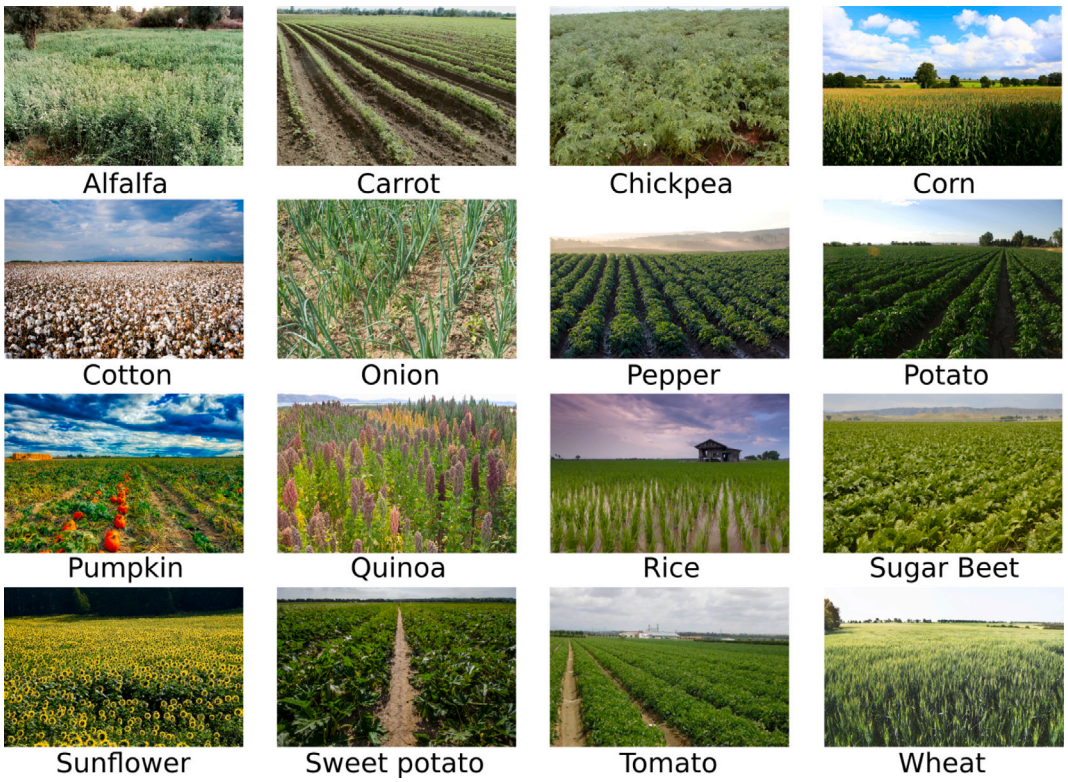

Fig. 2. Photographs of the studied crops during their growing season.

2.1.2. Sentinel-1 data

All available products for 2017 from the S1 A/B satellite constellation in interferometric wide swath mode, with polarisations VV and VH, have been used (Fig. 4). There are a total of 61 images for each one of the 3 relative orbits that cover the test site: orbits 74, 147 and 154 (Table 2). All have been considered in the study in order to test the influence of incidence angle and acquisition time, since they change for the different orbits. The original image resolution is approximately

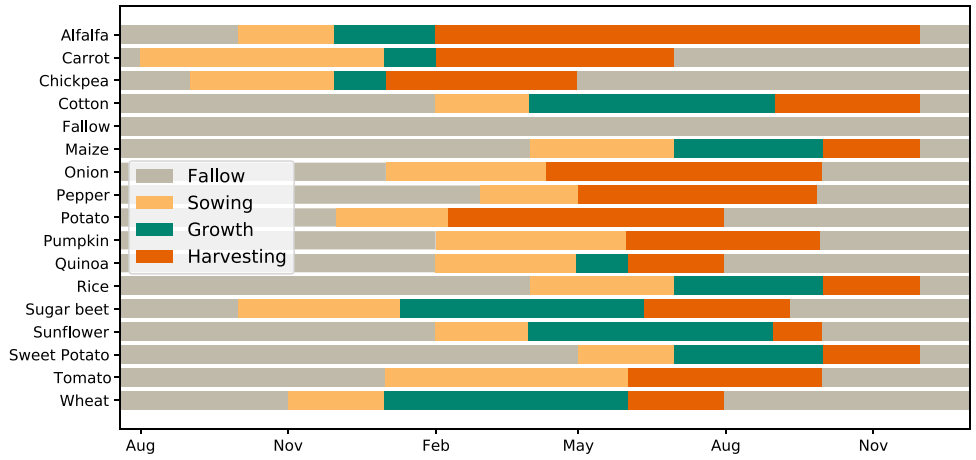

Fig. 3. Approximate crop calendar in the region.

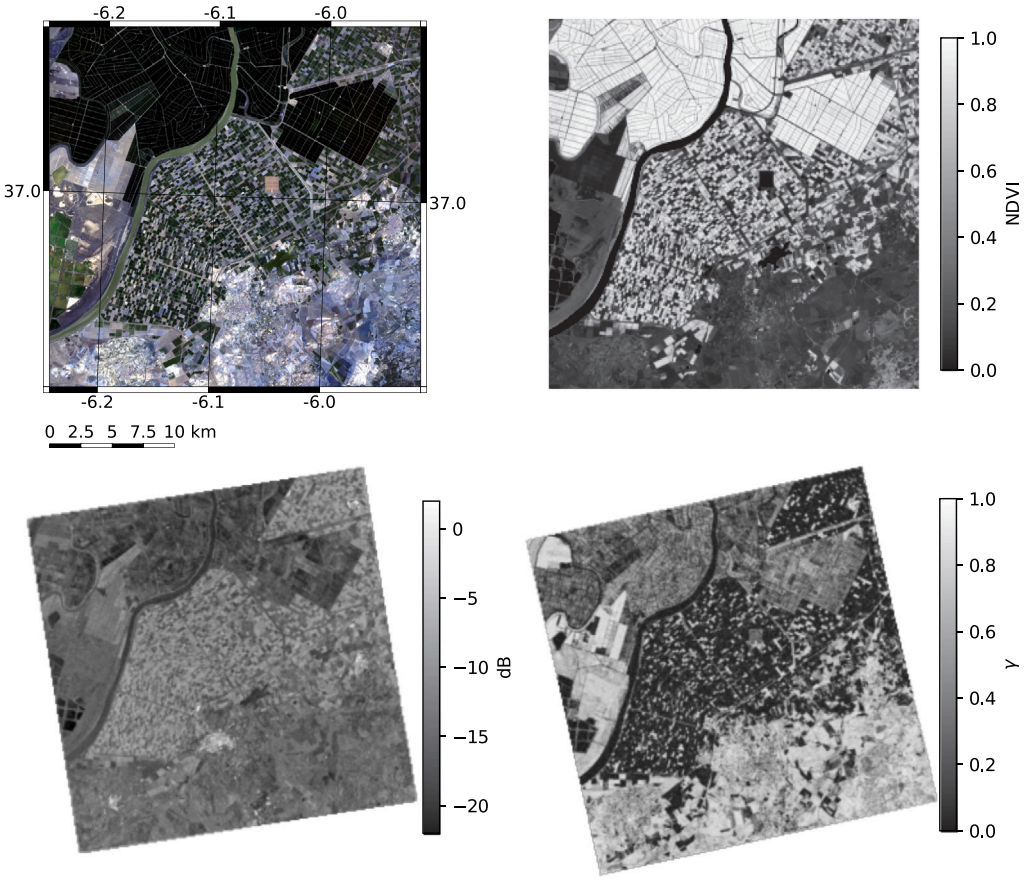

Fig. 4. Examples of S1 and S2 images over the study area. On the top left, an RGB composition with the red, green and blue bands from the S2 image for the 5th of August of 2017. For clear visualisation, the image has been subjected to a histogram equalisation. On its right, the corresponding NDVI image for the same date. On the bottom left, σ_0 (dB) at the VH channel measured on the 7th of August. On the bottom right, the coherence amplitude image for the VV channel between the 1st and 7th of August.

2.7 m x 22 m in slant-range range and azimuth, respectively, with a pixel size of 2.33 m x 14 m.

2.1.3. Sentinel-2 data

Reflectance images with Level-2 A processing from both S2 A and 2B have been used (Fig. 4). Despite the revisit time being 5 days, only 33 partially or completely cloud-free images were available for 2017. Particularly, the images correspond to tiles 29SQA and 29SQB, from orbit 137. The S2 images present a 10 m spatial resolution and were acquired between 11:00 and 11:20 a.m.

2.2. Processing

The overall processing scheme followed with all the satellite data is divided into the steps shown in Fig. 5. Since this work is focused on the exploitation of interferometric coherence, the main input data correspond to the time series of S1 images in SLC format. However, we also

Table 2
Characteristics of the available S1 orbits. Observation angle refers to the zenith angle.

Orbit	Flight direction	Subswath	Observation angle	Acquisition time
74	Ascending	IW1	31.5 - 33.5°	6 p.m.
147	Ascending	IW3	42.5 - 44.5°	6 p.m.
154	Descending	IW2	38.5 - 40.3°	6 a.m.

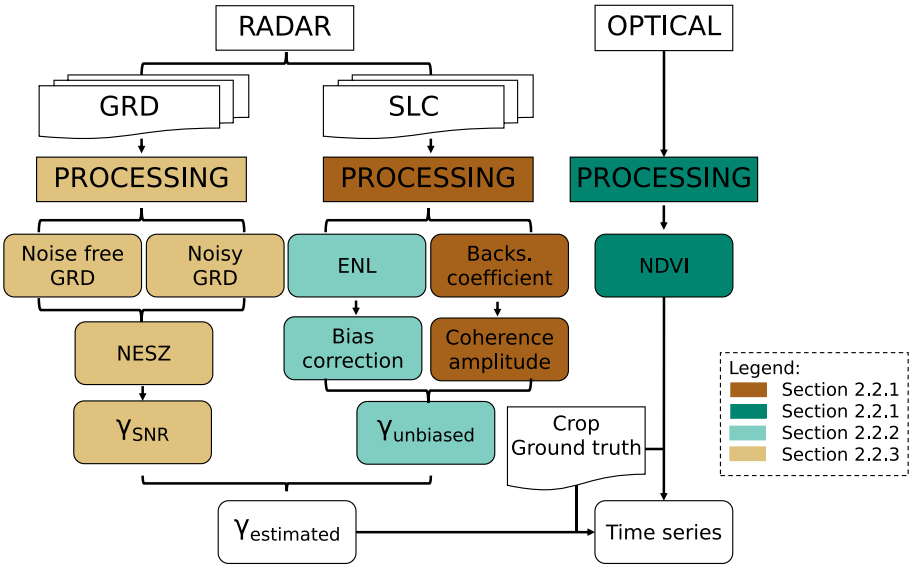

Fig. 5. Sentinel-1/2 processing workflow. The processing steps for the SLC (shown in brown in the diagram) and optical images (dark green) are discussed in Section 2.2.1. Section 2.2.2 describes the bias correction for the measured interferometric coherence (light green). Finally, the processing of the GRD images to obtain γ_{SNR} is explained in Section 2.2.3. (For interpretation of the references to colour in this figure legend, the reader is referred to the web version of this article.)

used S1 images in GRD to simplify the computation of noise, as it will be explained in Section 2.2.3. In addition, S2 images were employed for the computation of the NDVI. The pre-processing steps for the SLC and optical images are described in Section 2.2.1. Section 2.2.2 describes the bias correction for the measured interferometric coherence.

2.2.1. *Pre-processing*

The pre-processing steps of the SLC images are the following ones:

1. Selection of the desired sub-swath and bursts, using *TopSAR Split* tool.
2. Refining of the orbit state vectors using *Apply Orbit File*.
3. Radiometric calibration, with complex output.
4. Coregistration of the images using the *S-1 Back-geocoding* tool.
5. Speckle filtering and estimation of interferometric coherence.
6. Geocoding.

In the coregistration step, all the images of the 1-year long time series were coregistered with respect to the image in the middle of the year, which acted as *primary* or reference image. Later, for the computation of the coherence, the previously co-registered images were considered in pairs of chronologically ordered consecutive dates. For each pair, the first image and the second image were used as the *primary* and *secondary* image of each interferogram, respectively. All the steps but the speckle filter were carried out using ESA SNAP toolbox,[1] whereas the speckle filtering was undertaken with python routines. A boxcar filter of 19 samples in range and 4 samples in azimuth was used, as it is justified in Section 2.2.2. Since one dimension of the kernel was not an odd number, the boxcar filter implemented in SNAP could not be used. As a result of the SLC pre-processing, series of backscattering coefficient (σ_0) and coherence (γ) were obtained.

[1] https://step.esa.int/main/toolboxes/snap/

Additionally, a series of different radar vegetation indices for dual-polarimetric data were computed: the backscattering ratio (VH/VV), the Radar Vegetation Index (RVI, Mandal et al., 2021), the Dual-pol Radar Vegetation Index (DpRVI, Mandal et al., 2020a), the Dual-pol Radar Vegetation Index for GRD data ($DpRVI_c$, Bhogapurapu et al., 2022); and other descriptors defined for GRD data: the co-pol purity parameter m_c, the pseudo scattering type parameter θ_c, and the pseudo scattering entropy parameter H_c (Bhogapurapu et al., 2021). From all of them, only the DpRVI requires the use of S1 images in SLC format as input data, whereas the rest of indices are based on the backscattering coefficient values (i.e., power or intensity) and hence can be derived from S1 images in GRD format.

As for the S2 images, the processing was carried out also in ESA SNAP toolbox, and it consisted of the following steps:

1. Cloud masking, using the cloud mask layer provided by the product.
2. Mosaicking of the two adjacent tiles.
3. Computing the NDVI, using bands 4 and 8, corresponding to near-infrared and red wavelengths respectively.

Therefore, the output product of the processing of S2 images correspond to time series of NDVI images.

2.2.2. *Coherence estimation and bias*

Interferometric coherence constitutes the main feature in this study. It is defined as

$$\gamma = \frac{|E(s_1 s_2^*)|}{\sqrt{E(|s_1|^2) \cdot E(|s_2|^2)}} \quad (1)$$

where $E(x)$ represents the expected value of x, and s_1, s_2 are two complex signals (i.e., the two SLC images).

Its estimation is carried out by using the sample coherence magnitude, which represents the maximum likehood estimate of the coherence magnitude (Touzi et al., 1999). Given L signal measurements, the sample coherence magnitude is calculated as shown in Eq. (2):

$$\gamma_{est} = \frac{\left|\sum_{i=1}^{L} s_{1i} s_{2i}^{*}\right|}{\sqrt{\sum_{i=1}^{L}|s_{1i}|^2 \cdot \sum_{i=1}^{L}|s_{2i}|^2}}. \tag{2}$$

Unfortunately, this is a biased estimator, whose bias depends on the actual coherence magnitude. From the expression for its probability density function, the moments of order k can be derived as a function of the actual coherence magnitude γ. The case $k = 1$ corresponds to the first moment, which is its expected value:

$$E(\gamma_{est}) = \frac{\Gamma(L)\Gamma(3/2)}{\Gamma(L+1/2)} \cdot {}_3F_2\left(3/2, L, L; L+1/2; 1; \gamma^2\right) \cdot (1-\gamma^2)^L \tag{3}$$

where ${}_3F_2$ is the generalised hypergeometric function, and L represents the equivalent number of looks (ENL). The ENL can be used as an indicator of speckle noise (Lee and Pottier, 2009).

The estimated coherence γ_{est} is biased for low coherence values, where it takes higher values than the actual γ, thus causing a loss in contrast in areas with low coherence. The bias decreases when the number of independent samples (i.e. looks) is increased, as the estimator is asymptotically unbiased (Touzi et al., 1999).

As it was outlined in the Introduction, vegetation produces a strong temporal decorrelation, so the coherence that will be present during the crop growing season will be very low in many cases. As a result, if one wants to keep sensitivity to subtle changes of coherence due to vegetation condition, the mentioned bias needs to be carefully considered. The first implication is that the ENL needs to be high enough to reduce the impact of the bias. Unfortunately, increasing ENL degrades the spatial resolution, so a trade-off solution is required. This question was studied with the same type of data during the ESA-funded SInCohMap project (Jacob et al., 2020), and a 4x19 kernel for the boxcar filter was found as an optimum balance between resolution preservation and coherence estimation. Consequently, the same strategy has been followed in this work. Alternatively, Nikaein et al. (2021) proposed the use of a estimation kernel defined by the parcel boundaries, for which the available polygons in the reference data could be exploited.

In this work, since we know that the actual coherence can be very low, we have also explored the option of compensating the bias. For this purpose, the value of ENL is required. One possibility consists in measuring the ENL from the images themselves. Eq. (4) provides the ENL for a homogeneous area in an intensity SAR image, which is computed using the ratio of the standard deviation σ_x and the mean $\hat{x}$ for correlated pixels:

$$ENL = 1/\beta^2 \; ; \; \beta = \frac{\sigma_x}{\hat{x}} \tag{4}$$

For our study site, the ENL has been evaluated by selecting a homogeneous area in the coast, close to the site. A single date, January 8 or 9, depending on the orbit, was chosen. As the processing is the same for every image in the time series, and, particularly, the window used is always 4x19, the ENL values obtained have been used for all the series. It is important to note that the ENL would be different if a different filter size had been used during the processing. The ENL obtained is between 41 and 44 for both the VV and VH channels. Using a value ENL=41 and Eq. (3), the curve that relates the biased and the actual coherence was obtained (Fig. 6). Fig. 6 can be used to estimate the unbiased coherence magnitude from the measured sample coherence. Hereafter, these values will be referred to as $\gamma_{unbiased}$ and γ_{biased}, respectively.

2.2.3. Coherence terms

The interferometric coherence between a pair of SAR images can be expressed as the product of different contributions, which represent the decorrelation produced by different sources (Zebker and Villasenor, 1992; Bamler and Hartl, 1998):

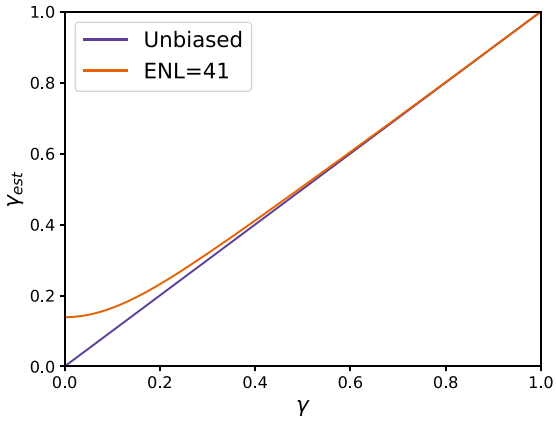

Fig. 6. Coherence magnitude bias for ENL=41. The reference unbiased line is what would result from using an infinite number of looks. It can be observed how the bias is present mostly for small coherence values.

$$\gamma = \gamma_{proc}\gamma_{geom}\gamma_{vol}\gamma_{SNR}\gamma_{temporal} \tag{5}$$

where each term has a value between 0 and 1, and γ represents the total interferometric coherence. In this case, it corresponds to the coherence after the compensation of the bias, $\gamma_{unbiased}$.

The first term in this expression, γ_{proc}, is referred to inaccuracies in the processing, e.g. coregistration errors, which may affect the interferometric products. The processing undertaken in this study, based on SNAP, guarantees that these errors are not present or are negligible, and this term can be directly eliminated.

The second term, denoted as γ_{geom}, represents the so-called geometrical or baseline decorrelation. Due to the different position of the satellite in the two acquisitions, the difference in incidence angle generates a loss of coherence which is directly proportional to the baseline (spatial distance between the two orbital positions). In the case of S1 the orbits are quite stable and the baselines are small (normally below 150 m), so this term can be neglected, i.e. $\gamma_{geom} \approx 1$.

The third term, known as volume decorrelation γ_{vol}, is present wherever there are more than one scatterer in the same pixel located at different height. Therefore, it is very characteristic of vegetation scenarios, i.e. forest and agricultural crops. However, as in the case of the geometrical decorrelation, its value strongly depends on the baseline. When the baseline is short and the vegetation is also short (crops rarely grow up to 3 m), the interferogram is not sensitive to the height differences in the scene, and volume decorrelation can be discarded, i.e. $\gamma_{vol} \approx 1$.

The remaining two terms will be the most relevant for this study. After the previous assumptions, the unbiased coherence can be expressed simply as:

$$\gamma_{unbiased} = \gamma_{SNR}\gamma_{temporal} \tag{6}$$

The term γ_{SNR} describes the influence of the thermal noise present in the radar instrument, and it depends on the signal-to-noise ratio (SNR) measured at each pixel. This term can be readily expressed as:

$$\gamma_{SNR} = \sqrt{\frac{SNR_1}{SNR_1+1}}\sqrt{\frac{SNR_2}{SNR_2+1}} \tag{7}$$

where the subscripts 1 and 2 refer to the two images of the pair. Since the noise is independent from the scene, the presence of thermal noise is noticeable especially in areas of low backscatter, i.e. areas with low SNR.

Using the same expression, the SNR decorrelation can be estimated from the data in the following way:

$$\gamma_{SNR} = \sqrt{\frac{S_1 - NESZ_1}{S_1}}\sqrt{\frac{S_2 - NESZ_2}{S_2}} \tag{8}$$

where S_i is the measured power or intensity of each image (i.e. measured backscattering coefficient), and $NESZ_i$ denotes the *Noise Equivalent Sigma Zero*, which indicates the noise floor of the image.

The value of $NESZ$ depends on the antenna pattern, and, in a multi-swath acquisition mode, shows different values in each sub-swath. For instance, Vincent et al. (2017) offers information about the NESZ for each sub-swath of the S1 satellites. In addition, the metadata and annotations of the S1 products include noise estimations (in form of polynomial coefficients) which can be employed to estimate the $NESZ$ present at each pixel in the images. Unfortunately, the interpretation and usage of these annotated polynomials is not straightforward.

In this study we have used a different method to estimate the $NESZ$ values, which consists in processing the same images, but in GRD format, and with two different processing chains as it is detailed next. The first processing consists of the following steps: *TopSAR Split*, *Apply Orbit File*, *Thermal Noise Removal*, *Assembly Orbit*, *Subset*, *Calibration*, *Speckle filtering* and *Geocoding*. Then, the second processing follows the same steps but the *Thermal Noise Removal* step was omitted. Finally, the $NESZ$ for each image is calculated as:

$$NESZ = GRD_{noisy} - GRD_{noisefree} \tag{9}$$

where $GRD_{noisefree}$ denotes the backscattering coefficient resulting from the first processing (with the *Thermal Noise Removal* step), and GRD_{noisy} denotes the backscattering coefficient resulting from the second processing (without the *Thermal Noise Removal* step).

In order to validate this method, the range of NESZ values obtained was compared to the estimations provided by Vincent et al. (2017). From this point, γ_{SNR} can be computed using Eq. (8). This methodology (estimating the SNR decorrelation factor for the coherence) was preferred to removing noise from the SLC images using the SNAP noise removal process. The reason is that the *Thermal Noise Removal* for SLC images is applied in SNAP to the SLC values, i.e. with speckle, and hence many values were found to fall below the estimated noise level (and not corrected).

Once the term γ_{SNR} is known, $\gamma_{temporal}$ can be obtained from the unbiased coherence $\gamma_{unbiased}$, resorting to Eq. (10):

$$\gamma_{temporal} = \frac{\gamma_{unbiased}}{\gamma_{SNR}} \tag{10}$$

This last term is the *temporal scene coherence* and represents the decorrelation caused by changes in the scene during the time interval between the two images that form the interferogram. In the study area, most of these changes can be attributed to vegetation features (plant growth, wind-induced movement of leaves and branches), water content (both in the soil and the vegetation canopy), and agricultural processes (ploughing, sowing, harvesting, etc.). Another important cause of temporal decorrelation is the change in the surface scattering due to rainfall events (this effect is reviewed in more detail in Section 3).

3. Results

3.1. Pre-processing of the coherence time series

The results displayed in this first section correspond to the S1 data from orbit 74. After the image processing outlined in Section 2.2.1, the reference ground truth data have been used to identify the coherence values for pixels corresponding to each crop type across the study area. The coherence values at all pixels of each crop type are used to build the corresponding time series. The mean value and the standard deviation on each date, computed from all pixels of each crop type,

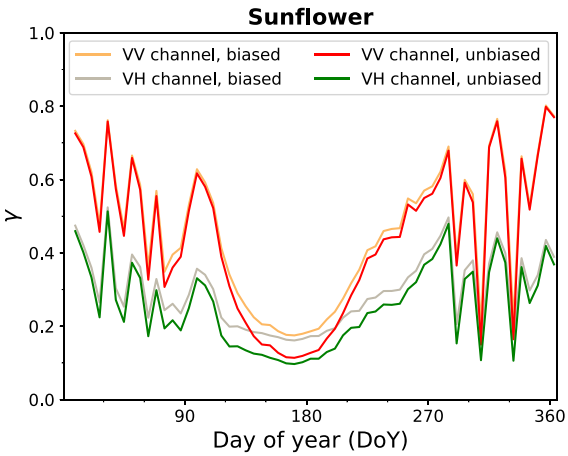

Fig. 7. Example of the time series for γ_{biased} and $\gamma_{unbiased}$ at both polarimetric channel for one crop type (sunflower).

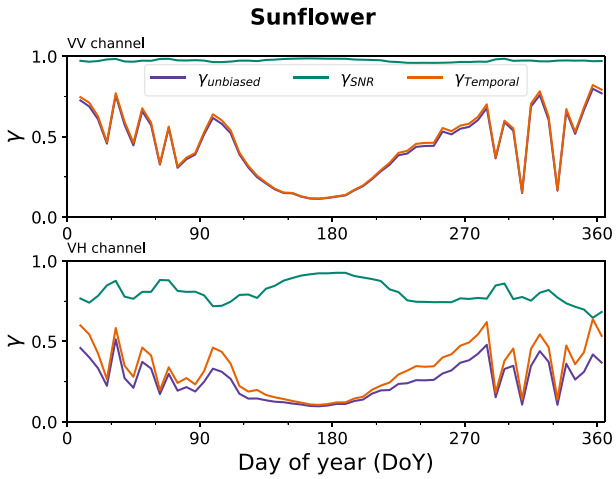

Fig. 8. Example of time series for $\gamma_{unbiased}$ and its components at each channel: γ_{SNR} and $\gamma_{temporal}$.

are represented in Figs. 10 to 13. The result is the series of measured coherence values throughout the year.

As shown in Eq. (3), the unbiased coherence $\gamma_{unbiased}$ can be estimated as a function of the measured, biased coherence γ_{biased}. Fig. 7 shows how the two time series differ for low coherence measurements and present similar values when the interferometric coherence increases. This can be observed for both polarimetric channels.

For the same case, the two main components of the coherence are shown in Fig. 8. At the VV channel, γ_{SNR} is mostly constant and approximately 1, so the measured coherence is mainly dependent on temporal decorrelation. At the VH channel, the signal received from the scene is always lower than at VV, therefore noise has a stronger effect. Only at the middle of the year (around DoY 180), when the plants are fully developed, the VH backscatter is large enough to minimise the effect of noise.

In both Figs. 7 and 8, there are abrupt changes in the values of coherence at the beginning and end of the year. These are caused by changes on the scene, and hence on the radar data, due to rainfall events. The effects are most evident at dates where the surface has little or no vegetation coverage, which is why the fluctuations appear outside the crop growth cycle. By using the daily rainfall archives, these data have been removed from the time series, hence smoothing the curves (see Fig. 9). The criterion used for removal of data was to eliminate the acquisition dates for which there had been one or more rain events

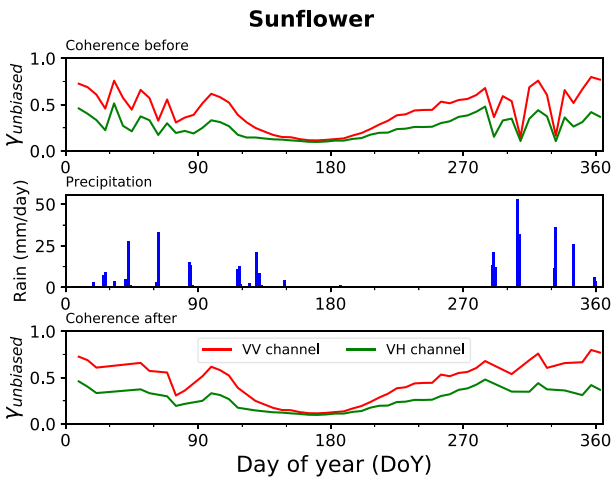

Fig. 9. Change in the time series after the removal of data for dates around rainfall events. From top to bottom: γ before filtering, recorded precipitation data, and γ after filtering.

(with more than 10 mm of cumulative precipitation) in the previous 2 days.

All these processing steps, i.e., bias compensation, SNR compensation, and rainfall dates removal, have been applied to all series of coherence in order to better interpret and exploit the information content of this radar feature on the crop properties and its dynamics.

3.2. Time series by crop type

After the processing described in Sections 2.2 and 3.1, the coherence time series for each crop type in the study area have been obtained. The time series of unbiased coherence of the two polarimetric channels, and their difference, are represented in Fig. 10 for all crop types. These correspond to the results for orbit 74. Analogous curves were obtained for the data from orbits 147 and 154. The plotted lines correspond to the mean coherence values for each date, while the shaded areas represent the corresponding standard deviation. The x-axis in this figure is kept as time (day of year), i.e., the values are represented at their corresponding acquisition dates. Other figures shown later to display time series follow the same criterion.

For most crops the time series presents rather constant coherence values at the beginning and end of the year, since there are little changes in the fields. These stable periods are separated by a "valley" that corresponds to the decrease in coherence caused by the presence and growth of vegetation during the crop growing season. The middle of this valley corresponds to the period of maximum development of the crop. It is important to note that the mere presence of vegetation induces temporal decorrelation, but also the crop growth, which entails changes in the dielectric structure of the plants, contributes to the observed low coherence values.

This curve is typically not symmetrical due to different reasons. In first place, the initial vegetative stages and the maturation-senescence period are usually characterised by a different duration. In second place, although it depends on the crop type, in many cases the initial growth stages correspond to a progressive increase of vegetation elements and their size (e.g. stem elongation), hence covering more the ground and reducing progressively the soil response. In contrast, harvesting is a sudden removal of most of the vegetation, thus producing a fast increase of coherence in later dates. However, the irregularities and stretching in the periods of decrease and increase of coherence can be understood also by considering that the values shown are an average for all the pixels in the study area, and not all the fields are planted or harvested at the same time.

Regarding the coherence difference between channels, the curve approaches zero during the maximum growth interval of the crops. At that stage both coherences are so low that they fall below the minimum measurable coherence due to the finite ENL. Consequently, there is no difference between them.

These curves replicate the behaviours seen in previous works (Pandit et al., 2022), where it was observed how the profile of the coherence was consistent with crop phenology: initial high coherence values correspond to highly exposed soil, the lowest point corresponds to the peak vegetative stage, and the later increase in coherence matches the maturation and senescence of the crop. Another observation that is corroborated in this case, is that coherence values after harvesting differ for each crop, probably due to differences in harvesting methods. Examples of these differences are cotton, maize and wheat, where the harvesting process implies cutting the whole plant, or alfalfa, where the crop is not cut completely at once. For the case of the tomato, however, the curves in Fig. 10 do not show the steady increase in coherence seen in (Pandit et al., 2022). This is also due to the difference in harvesting methods: plunking the tomatoes from the plants and then cutting the plants afterwards versus collecting the whole plant with a harvester in the case of these fields in Sevilla. As observed by Nasirzadehdizaji et al. (2021), apart from the dates of maximum growth, the coherence values are higher for the VV channel than for the VH. This difference is particularly significant in the period after harvesting. The backscatter at the VV comes partially from the ground, hence showing a more stable response, i.e. less affected by temporal decorrelation. Moreover, as we will see next, the backscattering coefficient at the VV channel is always greater than at the VH channel, so the SNR is also higher and, consequently, there is less decorrelation due to thermal noise in the VV channel.

The measured time series of backscattering coefficient (VV and VH) and NDVI are shown in Figs. 11 and 12, respectively. They have been constructed in the same way as the coherence time series, as described in Section 3.1. As one the of the most used radar vegetation indices, the ratio between channels is also computed and shown in Fig. 11. In the case of the backscattering, the expected behaviour is observed: the VV channel has a higher level than the VH, and the values of σ_0 increase during the growing season. Sowing, growth, and harvesting dates differ for each crop (Fig. 3), giving each curve characteristic features. These different behaviours allow for the use of radiometric and inferferometric data for crop classification, as it was exploited by Mestre-Quereda et al. (2020). One singular case is cotton. Both VV and VH rise at the same time and almost equally. A possible explanation for this could be that the plants grow in a structured way, and not by adding more and more randomly oriented elements (branches, tillers and leaves) as in most crops. In addition, as with other crops, the size of cotton leaves is similar to the C-band wavelength. For this reason, they are not characterised by Rayleigh scattering. The conjunction of both aspects is probably the reason of such a particular radar response from cotton. The ripple observed in the backscattering time series, especially in the ratio, is due to a known calibration difference between the two S1 sensors (A and B). Their alternation in the time series produces this effect, which is also reported in previous works (Khabbazan et al., 2019; Palmisano et al., 2021). In the case of the NDVI time series, the evolution in the curves responds to variations in the spectral properties of the scene (changes in its reflectivity) as well as its texture (degree of vegetation cover).

Despite describing different physical properties of the observed surface, there are clear similarities between the sets of time series of coherence, backscatter, and NDVI. This is an incentive to study the correlation between them, and, in the case of the coherence, explore the option of using it in a similar way as the already existing vegetation indices. To better illustrate this similarity, Fig. 13 presents all the curves together for four different crop types.

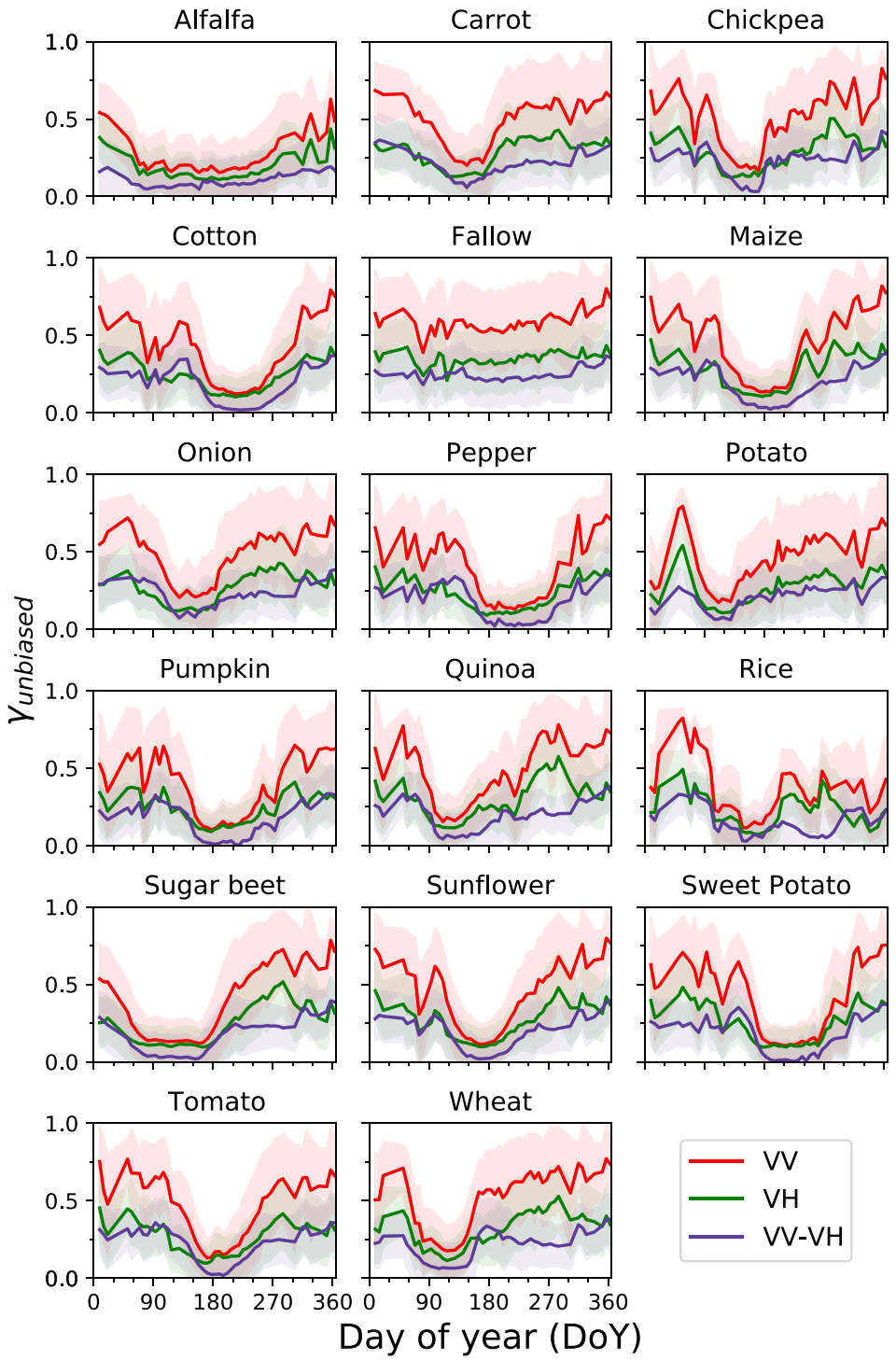

Fig. 10. Time series of unbiased coherence at VV and VH channels, and their difference, for all the different crop types in the case of orbit 74. The average at each date is represented by a continuous line, whereas the standard deviation is shown as a shaded area around the average.

3.3. Coherence as a vegetation index

In order to evaluate the potential of the interferometric coherence as a vegetation index, in this section it is compared quantitatively with the NDVI and with the backscattering ratio (VH/VV). The comparison has been performed through an analysis of the linear correlation between the radar time series and the NDVI time series. The coefficient of determination (R^2) is obtained for all cases.

In previous sections we have seen that the coherences measured at both channels, as well as their difference, show a clear temporal pattern that resembles the NDVI evolution, yet with a different dynamic range and/or sign, so the three of them will be evaluated. Moreover, we have also explained how the measured coherence can be modified by partially correcting its bias and by compensating the estimated thermal noise decorrelation. Therefore, it is convenient to test whether these processing steps are useful to better exploit coherence as a vegetation index. To this aim, the correlation analysis will be carried out separately for the measured (biased) coherence, the unbiased coherence, and the temporal coherence (i.e., after removing the thermal noise decorrelation).

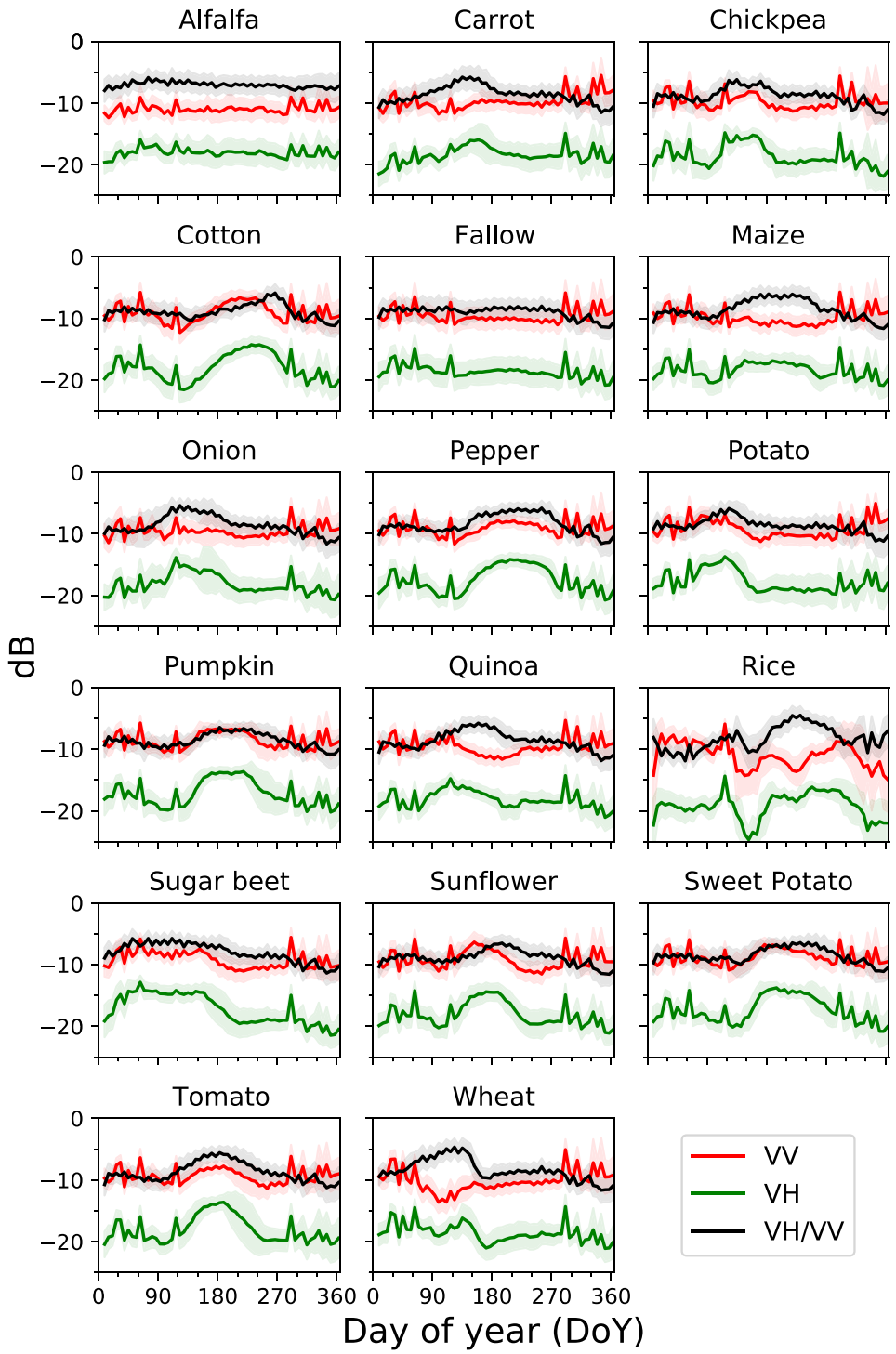

Fig. 11. Time series of σ_0 at VV and VH channels, and their ratio, all expressed in dB, for all the different crop types in the case of orbit 74. The average at each date is represented by a continuous line, whereas the standard deviation is shown as a shaded area around the average.

The data points considered in each case have been limited to those within the time interval corresponding to the growing season of each crop. This interval has been determined by inspection, crop by crop, with help of the approximate crop calendar (Fig. 3). To be able to compare the data, the coherence and backscattering time series have been linearly interpolated to the dates with valid NDVI data. This was the preferred option because the radar time series exhibit better continuity, which leads to a simpler interpolation and, thus, with less unwanted artefacts. For illustration purposes, four examples of the scatter plot and the linear fitting between the time series are displayed in Fig. 14.

The number of points considered in the regressions are shown in Table 3. As the different time series are always interpolated to the NDVI, this information also applies to later regressions, discussed in Sections 3.3 to 3.6. The amount of points used guarantee the statistical significance of the results with high values for the coefficient of determination (R^2). For instance, when working with a confidence interval of 95% ($\alpha = 0.05$), having at least 10 points guarantees that a result where $R^2 = 0.40$ is statistically significant ($p = 0.0498$). When using 15

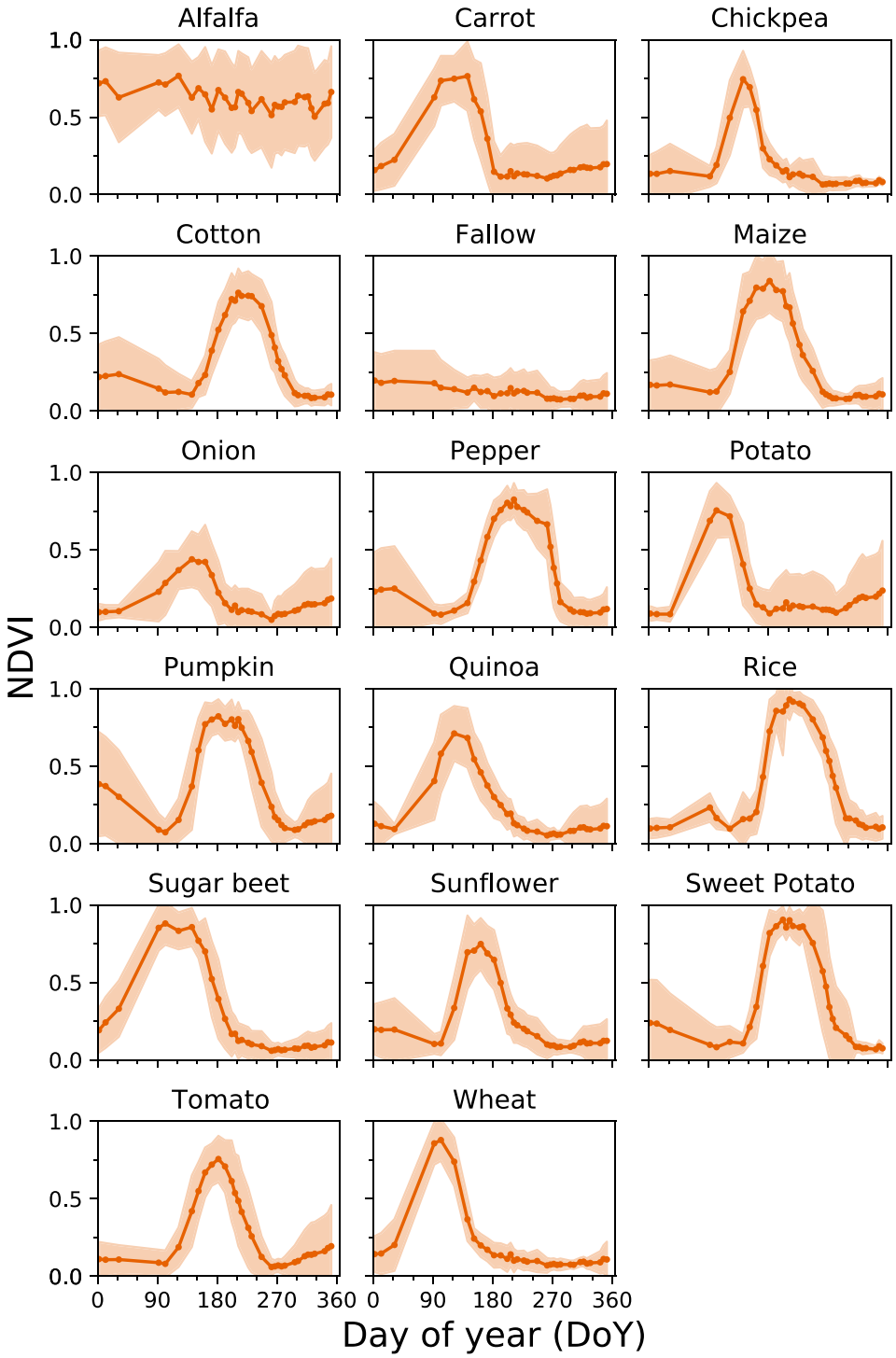

Fig. 12. Time series of NDVI for all the different crop types. The average at each date is represented by a continuous line, whereas the standard deviation is shown as a shaded area around the average.

or more points (the case for 14 out of the 16 crops), a regression with $R^2 = 0.30$ or higher is statistically significant ($p = 0.0348$).

The correlation results obtained are listed in Table 4 for orbit 74. The best results for each crop are highlighted in boldface. Fallow has not been considered in this analysis because it is not really a crop type. Therefore, the correlation analysis is restricted to 16 crop types.

A first inspection of Table 4 reveals that for 14 out of the 16 crop classes some of the coherence features present correlations with R^2 around or above 0.7. The exceptions are alfalfa and rice. Alfalfa is cultivated differently from other species because it has a multi-annual growing cycle and is harvested from time to time, and not for all fields at once. Consequently, as it was shown in Figs. 10, 11, and 12, the time series of all observations (radar and optical) of alfalfa are quite constant for the whole year. In the case of rice, coherence behaves differently with respect to the rest of the crops (see Fig. 10) because of the influence of the flooded ground, which reduces the coherence during the first part of the growing cycle (even before sowing). However, the backscattering coefficients show the typical increase when plants develop, and the backscattering ratio behaves as for most crops. In fact, the R^2 between NDVI and ratio is 0.80.

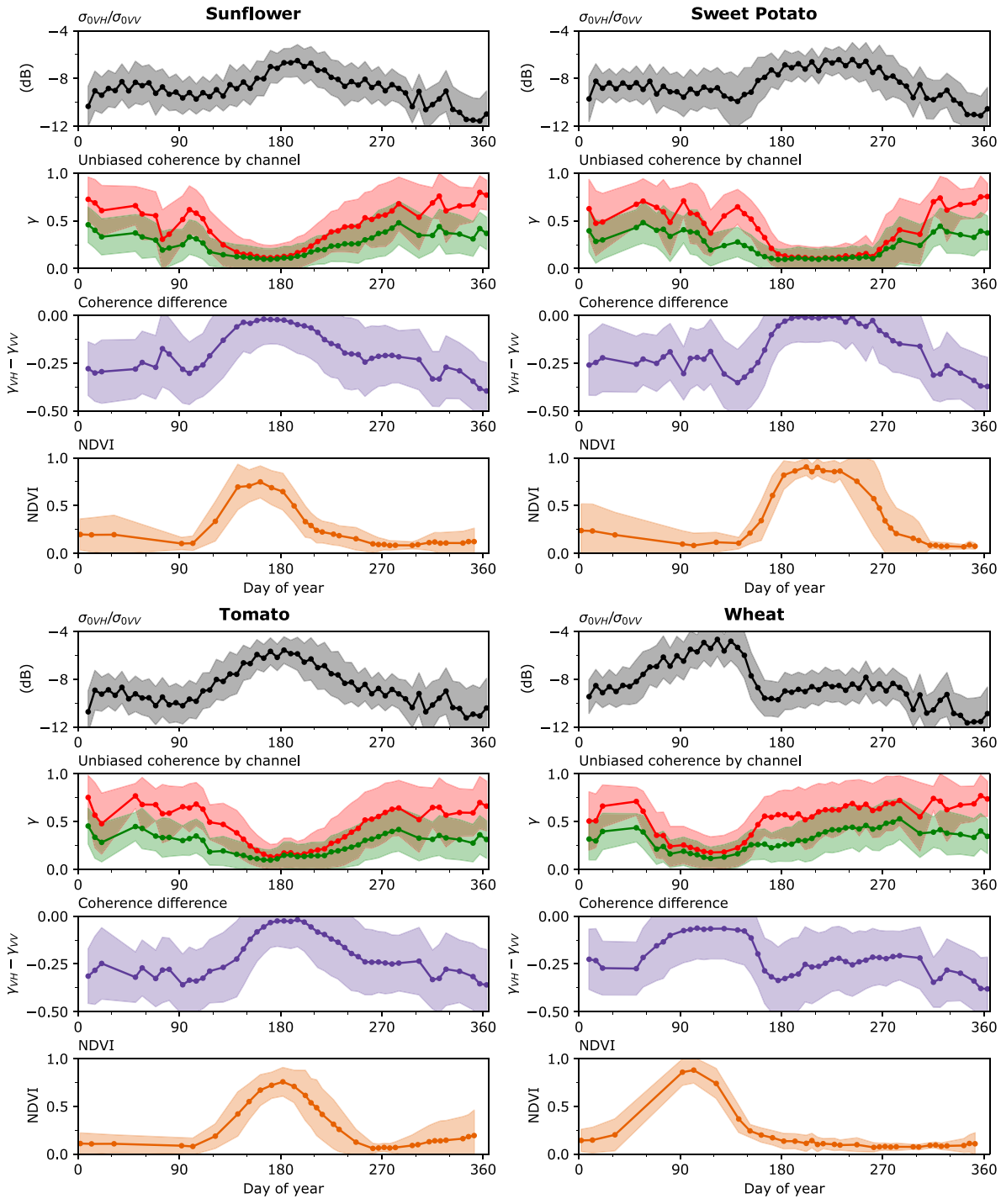

Fig. 13. Comparison of the different time series for certain crops. For each of the crops, the curves shown correspond to: (top) ratio of σ_0 for each channel, (centre) coherence for each channel and their difference, (bottom) NDVI.

Regarding the rest of the crops, the backscattering ratio shows R^2 values around or above 0.7 for 10 crops. However, it is poorly correlated with the NDVI in the case of cotton and sunflower. By inspection of Figs. 11–13, it can be seen how the time series for the backscattering ratio and the NDVI are not temporally aligned in these cases. In fact, the individual backscattering coefficient, especially VH, is better aligned with NDVI than the ratio. The reason for this is that the ratio is driven by differences in the pair of channels, as mentioned previously for the case of cotton.

Table 4 also tells us that the VV and VH coherences are more correlated to the NDVI than the difference between them and also more than the backscatter ratio.

Following the analysis of the results shown in Table 4, we observe that there are not noticeable differences among γ_{biased}, $\gamma_{unbiased}$, and $\gamma_{temporal}$ when studying each polarimetric channel separately, i.e., VV and VH. This means that the extra processing steps required to obtain them are not really needed to exploit the coherence as a vegetation index, what constitutes a good feature of this radar observable and facilitates its potential adoption for this purpose.

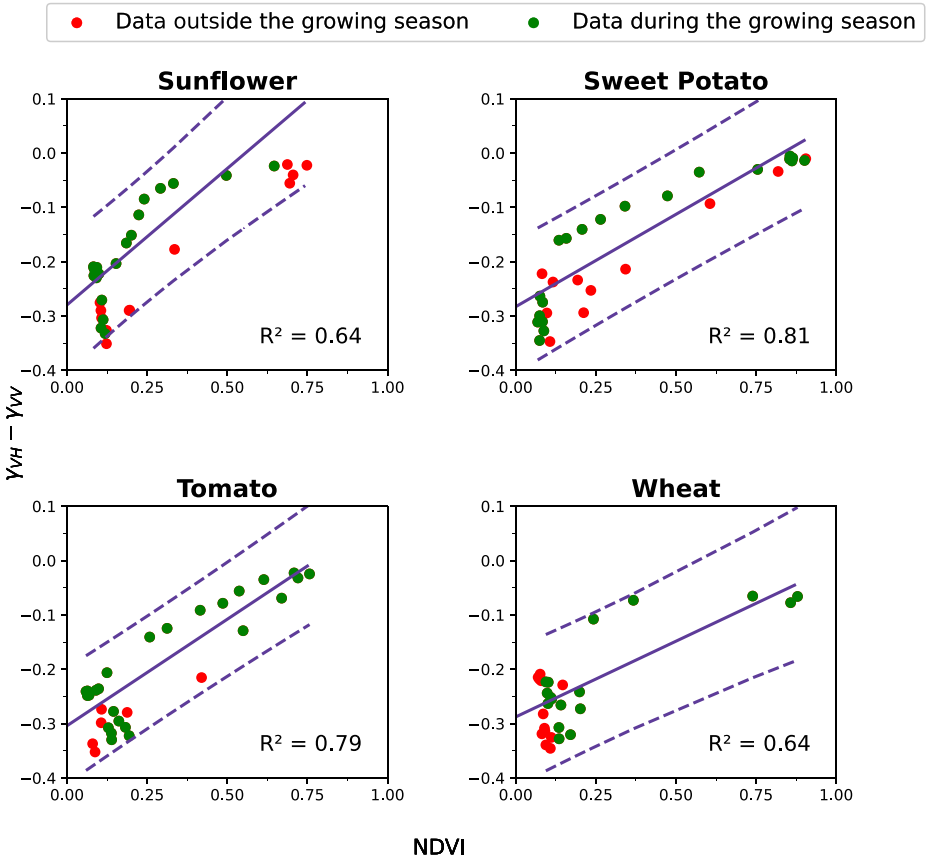

Fig. 14. Example of scatter plots between $\gamma_{VH} - \gamma_{VV}$ and NDVI, obtained for orbit 74. The linear fits between the two sets of data are shown in purple, with the dashed lines representing the confidence interval with a confidence level of 95%. The measured coefficient of determination R^2 for each case is displayed. To be able to establish a comparison between the two time series, with different acquisition dates, the coherence data was interpolated to the dates for the NDVI time series.

Table 3
Number of points used for the linear regressions discussed in Sections 3.3 and 3.6. These correspond to the number of data points in the NDVI time series inside each crop growth cycle.

	# of points		# of points
Alfalfa	23	Pumpkin	22
Carrot	15	Quinoa	16
Chickpea	15	Rice	19
Cotton	18	Sugar beet	18
Maize	22	Sunflower	15
Onion	12	Sweet Potato	24
Pepper	20	Tomato	29
Potato	10	Wheat	18

As for the coherence difference between channels ($\gamma_{VH} - \gamma_{VV}$), the selection of which coherence component to use has a clear impact on the correlation with NDVI. For most crop types (13 out of 16), the highest correlations with NDVI are obtained for $\gamma_{unbiased}$, usually followed by γ_{biased}, and with $\gamma_{temporal}$ exhibiting the worst correlation. On the one hand, addressing the bias for low coherence extends the range of values for both channels (Fig. 7), with a greater relative impact on VH, therefore helping to emphasise differences between them. On the other hand, removing the contribution from the thermal noise (to obtain $\gamma_{temporal}$) eliminates one of the two terms that provide sensitivity to the presence of vegetation: the signal-to-noise ratio. The fact that the SNR depends on the polarimetric channel, because the received power is different at VH and VV, makes the difference in SNR decorrelation at VH and VV sensitive to the crop growth. Consequently, when this term is compensated, the remaining difference is much less sensitive to the vegetation growth and, as a result, the correlation with NDVI is smaller than when the SNR is not compensated.

To understand the reason why the coherence is more correlated with the NDVI for a certain channel, the potential influence of differences in vegetation height, plant density, spatial homogeneity, and seasonality among crops has been considered. To begin with, results do not show any distinct trend for short or tall crop types. VV coherence is generally more correlated with the NDVI than VH coherence. This difference is smaller in the case of crops that present less density of plants or lower fractional vegetation cover, such as carrot, chickpea, onion, pepper, pumpkin, sweet potato and tomato. In some of these cases (carrot and onion), the VH channel shows higher correlation values. Regarding the influence of the dates of the growing season, it has been observed that having an incomplete time series for the NDVI may have a noticeable effect. The lack of data in February and March, due to clouds, results in part of the crops having lower correlations. Considering the dates for each growing season (Fig. 3), as well as Figs. 10 to 12, the crops that grow early in the year obtain lower correlation values than the rest. This is the case for carrot, chickpea, quinoa, sugar beet, sunflower and wheat. In contrast, the values for R^2 are higher for crops that reach maturity around the middle of the year (maize, onion, pumpkin, tomato) or later (cotton or pepper).

3.4. Comparison of satellite orbits

The correlation results obtained for the other two orbits are shown in Tables 5 and 6, which correspond to orbits 147 and 154, respectively. Despite providing values different to the ones measured at orbit 74, the overall comments are equally valid for these orbits. First, most crop types exhibit high correlation between the interferometric coherence (in any of its forms) and NDVI. Second, the coherence at individual channels is more correlated with NDVI than the difference between

Table 4
Coefficient of determination (R^2) for the linear regressions between the radar time series and the NDVI time series for orbit 74. The best results for each crop are highlighted in bold.

	VV			VH			VH–VV			$\sigma_{0VH}/\sigma_{0VV}$
	γ_{biased}	$\gamma_{unbiased}$	$\gamma_{temporal}$	γ_{biased}	$\gamma_{unbiased}$	$\gamma_{temporal}$	γ_{biased}	$\gamma_{unbiased}$	$\gamma_{temporal}$	(dB)
Alfalfa	0.01	0.01	0.01	−0.01	−0.02	0.00	0.07	**0.19**	0.08	0.20
Carrot	0.37	0.34	0.33	**0.66**	**0.65**	0.59	−0.02	0.10	−0.05	0.48
Chickpea	**0.68**	**0.68**	**0.68**	0.60	0.61	0.61	0.65	**0.69**	0.61	0.50
Cotton	**0.93**	**0.94**	**0.93**	0.84	0.85	0.87	0.83	0.84	0.86	−0.03
Fallow	–	–	–	–	–	–	–	–	–	–
Maize	**0.88**	**0.88**	**0.88**	0.75	0.76	0.81	0.74	0.78	0.60	0.68
Onion	0.65	0.64	0.64	**0.83**	**0.83**	**0.81**	0.35	0.46	0.23	0.79
Pepper	**0.89**	**0.89**	**0.89**	0.71	0.73	0.80	0.66	0.76	0.58	0.83
Potato	**0.92**	**0.91**	**0.92**	0.75	0.76	0.83	0.86	0.88	0.69	0.67
Pumpkin	**0.80**	**0.81**	**0.82**	0.77	0.78	0.79	0.71	0.78	0.65	0.76
Quinoa	**0.82**	**0.82**	**0.82**	0.68	0.68	0.76	0.61	0.72	0.44	0.39
Rice	0.18	0.19	0.20	0.07	0.09	0.03	0.16	0.09	0.39	**0.80**
Sugar beet	0.85	0.84	0.85	0.78	0.79	0.79	0.83	**0.91**	0.79	0.82
Sunflower	0.72	0.74	0.74	**0.77**	**0.78**	0.71	0.63	0.61	0.62	−0.02
Sweet Potato	0.78	0.78	0.78	0.72	0.73	0.77	0.67	**0.80**	0.65	0.77
Tomato	**0.85**	**0.84**	**0.85**	0.80	0.81	**0.85**	0.70	0.79	0.50	0.81
Wheat	**0.72**	**0.72**	**0.72**	0.52	0.54	0.59	0.61	0.63	0.47	**0.70**

Table 5
Coefficient of determination (R^2) for the linear regressions between the radar time series and the NDVI time series for orbit 147. The best results for each crop are highlighted in bold.

	VV			VH			VH–VV			$\sigma_{0VH}/\sigma_{0VV}$
	γ_{biased}	$\gamma_{unbiased}$	$\gamma_{temporal}$	γ_{biased}	$\gamma_{unbiased}$	$\gamma_{temporal}$	γ_{biased}	$\gamma_{unbiased}$	$\gamma_{temporal}$	(dB)
Alfalfa	0.05	0.05	0.05	0.03	0.03	0.04	0.16	0.29	0.20	**0.40**
Carrot	0.52	0.49	0.49	**0.71**	**0.70**	0.68	−0.01	0.07	−0.03	0.63
Chickpea	0.69	0.70	0.70	0.63	0.64	0.64	**0.73**	**0.72**	**0.72**	0.69
Cotton	**0.89**	**0.90**	**0.90**	0.87	0.88	**0.89**	0.67	0.68	0.67	−0.04
Fallow	–	–	–	–	–	–	–	–	–	–
Maize	**0.88**	**0.88**	**0.88**	0.83	0.83	0.85	0.61	0.62	0.51	0.66
Onion	0.74	0.74	0.74	0.79	0.79	0.78	0.48	0.57	0.45	**0.84**
Pepper	**0.84**	**0.84**	**0.84**	0.73	0.75	0.76	0.58	0.66	0.57	**0.85**
Potato	0.72	0.72	0.73	0.58	0.60	0.63	0.62	0.74	0.57	**0.82**
Pumpkin	**0.83**	**0.83**	**0.84**	**0.83**	**0.84**	**0.84**	0.70	0.76	0.69	0.76
Quinoa	**0.87**	**0.87**	**0.88**	0.73	0.73	0.78	0.61	0.63	0.50	0.40
Rice	0.07	0.09	0.10	0.06	0.07	0.02	−0.06	−0.06	0.08	**0.58**
Sugar beet	**0.87**	**0.87**	**0.87**	0.80	0.81	0.81	0.82	**0.89**	0.81	0.77
Sunflower	0.63	0.65	0.65	**0.70**	**0.71**	0.69	0.53	0.52	0.52	0.20
Sweet Potato	0.76	0.77	0.77	0.68	0.70	0.69	0.63	0.73	0.60	**0.82**
Tomato	0.83	0.83	0.83	0.79	0.80	0.79	0.67	0.74	0.56	**0.89**
Wheat	0.67	0.68	0.68	0.61	0.62	0.64	0.55	0.57	0.51	**0.70**

Table 6
Coefficient of determination (R^2) for the linear regressions between the radar time series and the NDVI time series for orbit 154. The best results for each crop are highlighted in bold.

	VV			VH			VH–VV			$\sigma_{0VH}/\sigma_{0VV}$
	γ_{biased}	$\gamma_{unbiased}$	$\gamma_{temporal}$	γ_{biased}	$\gamma_{unbiased}$	$\gamma_{temporal}$	γ_{biased}	$\gamma_{unbiased}$	$\gamma_{temporal}$	(dB)
Alfalfa	0.03	0.03	0.03	0.02	0.02	0.03	0.06	0.14	0.10	**0.26**
Carrot	0.27	0.25	0.26	**0.68**	**0.68**	**0.66**	−0.08	−0.07	−0.06	0.25
Chickpea	0.62	0.62	0.63	0.63	**0.64**	**0.66**	0.56	0.58	0.48	0.62
Cotton	**0.93**	**0.94**	**0.94**	0.88	0.89	0.91	0.82	0.83	0.87	−0.04
Fallow	–	–	–	–	–	–	–	–	–	–
Maize	**0.85**	**0.85**	**0.86**	0.82	0.83	**0.85**	0.61	0.66	0.54	0.74
Onion	0.75	0.74	0.75	**0.82**	**0.82**	0.80	0.38	0.43	0.25	**0.84**
Pepper	**0.81**	**0.82**	**0.82**	0.68	0.69	0.72	0.68	0.78	0.73	0.71
Potato	**0.83**	**0.84**	**0.85**	0.73	0.75	0.80	0.55	0.63	0.34	0.58
Pumpkin	0.75	0.75	0.76	**0.78**	**0.79**	**0.80**	0.59	0.69	0.61	0.65
Quinoa	**0.78**	**0.78**	**0.79**	0.74	0.73	**0.80**	0.31	0.34	0.12	0.38
Rice	0.09	0.11	0.10	0.04	0.05	−0.03	0.04	−0.04	0.24	**0.40**
Sugar beet	**0.83**	**0.83**	**0.83**	0.80	0.81	**0.82**	0.72	0.81	0.71	**0.82**
Sunflower	0.75	0.77	0.77	**0.82**	**0.83**	**0.82**	0.66	0.64	0.61	−0.08
Sweet Potato	0.75	0.74	0.74	0.69	0.70	0.71	0.48	0.57	0.42	**0.81**
Tomato	0.86	0.85	0.86	0.84	0.85	0.85	0.64	0.74	0.54	**0.90**
Wheat	0.65	**0.66**	**0.66**	0.57	0.59	0.64	0.53	0.52	0.38	**0.67**

channels. Third, the three versions of coherence (biased, unbiased, and temporal) perform equally for the individual channels.

It must be noted that the different acquisition conditions of the three orbits (Table 2) introduce changes in the coherence which need further explanation. In first place, the measurements for orbits 74 and 147 are done in the evening, when wind speeds are the highest in this geographical location (SIAR, 2022), whereas the images of orbit 154 are acquired at 6 a.m., which is a time in the day characterised by absence of wind.

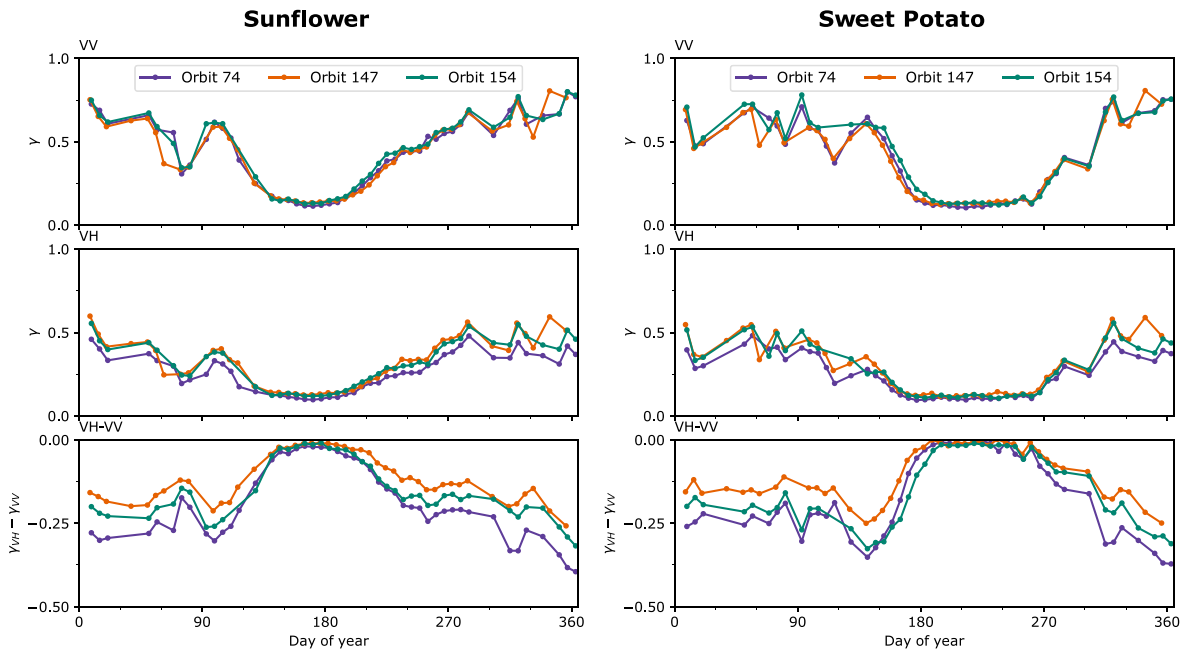

Fig. 15. Examples of coherence time series for different orbits. The curves correspond to $\gamma_{unbiased}$ for VH, VV, and VH–VV.

The presence of wind increases the temporal decorrelation caused by vegetation due to the movement induced in the plant elements. This should produce higher coherences for orbit 154 than for the other two. Additionally, each orbit has a different incidence angle (Table 2) which affects the combination or balance of radar responses from the vegetation and the ground. The smaller angles correspond to the steeper observations, for which there is more backscatter from the ground. Contrarily, the larger angles correspond to shallower incidences, for which the backscatter from the vegetation tends to dominate. As a result, one expects to measure higher coherence values at the steeper incidence angles, since the ground is more stable and hence less prone to temporal decorrelation. Regarding the backscattering ratio, the data measured at the shallowest incidence angle (orbit 147) are the most correlated with NDVI, which is a direct consequence of the mentioned balance of the vegetation and ground responses as a function of the incidence angle.

Fig. 15 exemplifies the effect of the observation conditions in the coherence measurements for two different crop types. The curves of each crop show qualitatively the same behaviour in all orbits: the increase and decrease of the curves occur at the same dates and with similar slopes, VH–VV is nearly zero (VV and VH are very similar) around mid-season, and they seem to share the same sources of fluctuations, evidenced by sharp changes in values outside the period of crop growth, for example, around days 75 and 315. However, there are some differences: the VH coherence of orbit 74 shows values lower than the other two orbits along the whole year, and when comparing the difference between channels, orbit 74 shows a wider range of values, followed by orbit 154, and then by orbit 147. In fact, while the values of the VH–VV difference of coherence approach zero during mid-season in all orbits, the difference between channels is bigger or smaller for each orbit at the early and late stages of the crop cycle. The different dynamic range has a direct effect on the observed correlations between coherence and NDVI.

To better compare the results of the three orbits, the R^2 values of all orbits are shown in Table 7 for the case of $\gamma_{unbiased}$. In general, when the observation is more vertical, the correlation with the NDVI improves. The steepest angle corresponds to orbit 74, with the best results. The observations for orbit 154 were performed during the morning, with nearly null wind speeds. Despite this potential benefit, orbit 74 remains as the best overall case.

3.5. Effect of the temporal baseline

While S1 offers a 6-day revisit time in Europe, its temporal resolution for most of the rest of the world is 12 days (Potin et al., 2021). Due to this, other similar studies (Nasirzadehdizaji et al., 2021; Pandit et al., 2022) have worked with a 12-day separation between images. Additionally, S1-B suffered technical problems on the 23rd of December of 2021, which caused it to stop operations. At the time of this research work, only images from S1-A are available, starting from that date.

For these reasons, the effect of changing from a 6-day to a 12-day temporal baseline has been assessed. In a process analogous to the steps described in Sections 3.1 and 3.2, the time series for a 12-day time interval have been built. For this, every second date from the data was chosen, as if only the images from one of the two satellites were available. The satellites used for each orbit were selected to have the images at the same dates, so the comparison among orbits is possible without side effects due to date differences between the acquisitions at different orbits. These time series were compared to the NDVI in the same way as described in Sections 3.3 and 3.4. The results in Table 8 show the correlation between the coherences measured with a 12-day separation and the NDVI. The differences between Tables 7 and 8 serve to illustrate how the temporal baseline affects the coherence in this scenario.

For the majority of the crops, the R^2 values decrease when using the 12-day interval, but for 9 crops the values are still around or above 0.7, hence keeping a clear sensitivity to crop growth. As expected, the increase in the temporal baseline reduces the coherence outside the period of maximum growth of the crop, whereas it is as low as in the 6-day case during the interval with full vegetation development. For this reason, there is a smaller dynamic range in the coherence values. In addition, some isolated changes detected with a 6-day coherence are missing in the 12-day case due to the reduced sampling rate. In some cases, the level of correlation with NDVI remains very high (R^2 above 0.85), such as for cotton, maize, tomato and sugar beet.

3.6. Use of other radar vegetation indices

The level of correlation between the ratio of backscattering coefficient at the two polarisation channels (VH and VV) and the NDVI has been examined in previous sections. The performance of the rest of the

Table 7
Coefficient of determination (R^2) for the linear regressions between the unbiased coherence ($\gamma_{unbiased}$) and the NDVI, for each orbit. The regressions with the NDVI have been performed for each interferometric channel and the difference between them. The best results for each crop are highlighted in bold.

	ORBIT 74			ORBIT 147			ORBIT 154		
	γ_{VV}	γ_{VH}	$\gamma_{VH}-\gamma_{VV}$	γ_{VV}	γ_{VH}	$\gamma_{VH}-\gamma_{VV}$	γ_{VV}	γ_{VH}	$\gamma_{VH}-\gamma_{VV}$
Alfalfa	0.01	−0.02	0.19	0.05	0.03	**0.29**	0.03	0.02	0.14
Carrot	0.34	0.65	0.10	0.49	**0.70**	0.07	0.25	0.68	−0.07
Chickpea	0.68	0.61	0.69	**0.70**	0.64	**0.72**	0.62	0.64	0.58
Cotton	**0.94**	0.85	0.84	0.90	0.88	0.68	**0.94**	0.89	0.83
Fallow	–	–	–	–	–	–	–	–	–
Maize	**0.88**	0.76	0.78	**0.88**	0.83	0.62	0.85	0.83	0.66
Onion	0.64	**0.83**	0.46	0.74	0.79	0.57	0.74	**0.82**	0.43
Pepper	**0.89**	0.73	0.76	0.84	0.75	0.66	0.82	0.69	0.78
Potato	**0.91**	0.76	0.88	0.72	0.60	0.74	0.84	0.75	0.63
Pumpkin	0.81	0.78	0.78	**0.83**	**0.84**	0.76	0.75	0.79	0.69
Quinoa	0.82	0.68	0.72	**0.87**	0.73	0.63	0.78	0.73	0.34
Rice	**0.19**	0.09	0.09	0.09	0.07	−0.06	0.11	0.05	−0.04
Sugar beet	0.84	0.79	**0.91**	0.87	0.81	0.89	0.83	0.81	0.81
Sunflower	0.74	0.78	0.61	0.65	0.71	0.52	0.77	**0.83**	0.64
Sweet Potato	**0.78**	0.73	**0.80**	0.77	0.70	0.73	0.74	0.70	0.57
Tomato	**0.84**	0.81	0.79	0.83	0.80	0.74	**0.85**	**0.85**	0.74
Wheat	**0.72**	0.54	0.63	0.68	0.62	0.57	0.66	0.59	0.52

Table 8
Coefficient of determination (R^2) for the linear regressions between the unbiased coherence with a 12-day temporal baseline and the NDVI for each polarimetric channel and each of the orbits. These results are analogous to those in Table 7, which correspond to the 6-day interval.

	ORBIT 74			ORBIT 147			ORBIT 154		
	γ_{VV}	γ_{VH}	$\gamma_{VH}-\gamma_{VV}$	γ_{VV}	γ_{VH}	$\gamma_{VH}-\gamma_{VV}$	γ_{VV}	γ_{VH}	$\gamma_{VH}-\gamma_{VV}$
Alfalfa	0.00	0.00	0.11	0.07	0.08	**0.21**	0.07	0.07	**0.23**
Carrot	0.17	0.54	0.12	0.39	**0.63**	−0.01	0.06	0.59	−0.08
Chickpea	0.51	0.31	0.54	0.52	0.41	**0.56**	0.43	0.34	0.53
Cotton	0.80	0.65	0.72	0.67	0.72	0.60	**0.82**	**0.86**	0.64
Fallow	–	–	–	–	–	–	–	–	–
Maize	0.79	**0.83**	0.66	0.77	**0.83**	0.51	0.77	**0.86**	0.53
Onion	0.50	0.77	0.50	0.66	**0.83**	0.41	0.54	0.69	0.36
Pepper	0.54	0.50	0.57	0.58	0.58	0.60	0.62	**0.78**	0.53
Potato	0.21	0.16	**0.53**	−0.02	−0.05	0.36	−0.02	0.19	0.03
Pumpkin	0.55	**0.68**	0.52	0.50	0.46	0.60	0.53	**0.67**	0.42
Quinoa	0.80	0.62	0.76	0.75	**0.81**	0.45	0.58	0.63	0.45
Rice	0.03	−0.03	−0.03	**0.10**	0.05	−0.05	−0.04	−0.02	−0.02
Sugar beet	0.74	0.59	**0.85**	0.80	0.72	**0.84**	0.72	0.68	0.78
Sunflower	0.57	0.57	0.50	0.49	0.49	0.44	**0.58**	0.56	0.54
Sweet Potato	0.58	0.62	0.59	**0.74**	0.63	**0.77**	0.58	0.70	0.41
Tomato	0.77	**0.84**	0.75	0.78	0.78	0.70	0.73	0.77	0.62
Wheat	**0.58**	0.36	**0.58**	0.54	0.45	0.48	0.55	0.46	0.54

backscatter-based radar VIs in this particular scope is analysed in this section. For this purpose, the R^2 values provided by the ratio (in both dB and linear scale) and the rest of radar VIs are included in Table 9.

It can be seen how the values for R^2 are quite similar for all the indices, with maximum differences below 0.1. In fact, the descriptors m_c, θ_c, H_c and $DpRVI_c$ are directly derived from the ratio in linear scale, and the differences between using $\sigma_{0VH}/\sigma_{0VV}$ in linear or logarithmic scale are negligible in most cases. On the other hand, the results for the DpRVI and the $DpRVI_c$ are identical. In summary, apart from small numerical differences, the main conclusions regarding the performance of the backscattering ratio can be adopted also for the rest of backscatter-based VIs.

4. Discussion

This work obviously constitutes an extension of previous studies in which repeat-pass coherence was explored for crop monitoring or classification. With respect to the early works in this domain (Wegmuller and Werner, 1997; Strozzi et al., 2000; Engdahl et al., 2001; Blaes and Defourny, 2003; Engdahl and Hyyppä, 2003) here we have exploited Sentinel-1 to gather a one-year long time series of coherence measured with a 6-day temporal baseline, hence using a much more complete dataset than those available with tandem ERS data, which consisted of only a few acquisitions. Regarding the more recent works based on Sentinel-1 data (Mestre-Quereda et al., 2020; Nikaein et al., 2021; Nasirzadehdizaji et al., 2021; Pandit et al., 2022), the additions are relevant in a wide range of aspects. The first and most important novelty is the quantitative characterisation of coherence as a vegetation index, for which its correlation with NDVI (the most widely used index) has been measured. The performance of coherence as a VI has been tested for 16 crop classes which comprise a large variety of vegetation features. Another novelty with respect to previous works is the analysis of the coherence measured at the two available channels, VV and VH, as well as their difference, in order to identify the most sensitive feature. In addition, the separation of the two decorrelation sources (thermal noise and temporal) which provide sensitivity to the crop growth has been undertaken for the first time for this purpose. In order to provide an exhaustive study on the applicability of S1 coherence as a vegetation index, the influence of the orbit, i.e. incidence angle and acquisition time, has been assessed by using 3 different datasets. Finally, the effect of the temporal baseline, i.e. 6 or 12 days, has been analysed. In summary, a significant number of new insights have been provided by this work with respect to the literature. The most relevant findings are discussed in the rest of this section.

To start the discussion of the results it is important to understand that optical and SAR imagery are based in different physical principles

Table 9
Coefficient of determination (R^2) for the linear regressions between different radar vegetation indices and the NDVI, for orbit 74. The best results for each crop are highlighted in bold.

	RVI	DpRVI	$DpRVI_c$	$\frac{\sigma_{VH}}{\sigma_{VV}}$ (dB)	$\frac{\sigma_{VH}}{\sigma_{VV}}$ (lin)	m_c	θ_c	H_c
Alfalfa	0,21	0,20	0,20	0,20	**0,22**	0,21	**0,23**	0,19
Carrot	**0,49**	0,48	0,48	0,48	**0,50**	**0,49**	**0,50**	0,46
Chickpea	0,50	0,50	0,50	0,50	0,47	0,50	0,44	**0,53**
Cotton	−0,05	−0,04	−0,04	−0,03	−0,06	−0,05	−0,06	−0,02
Fallow	–	–	–	–	–	–	–	–
Maize	**0,71**	**0,72**	**0,72**	0,68	0,70	**0,71**	0,69	0,70
Onion	**0,79**	0,78	0,78	**0,79**	**0,80**	**0,79**	**0,80**	0,77
Pepper	**0,86**	**0,86**	**0,86**	0,83	**0,86**	**0,86**	**0,86**	**0,86**
Potato	0,66	0,66	0,66	0,67	0,64	0,66	0,61	**0,69**
Pumpkin	**0,78**	**0,79**	**0,79**	0,76	**0,78**	**0,78**	0,77	**0,79**
Quinoa	0,38	0,38	0,38	**0,39**	0,37	0,38	0,36	**0,40**
Rice	**0,79**	**0,80**	**0,80**	**0,80**	**0,79**	**0,79**	0,78	0,78
Sugar beet	**0,85**	0,84	0,84	0,82	0,84	**0,85**	0,82	**0,86**
Sunflower	−0,03	−0,02	−0,02	−0,02	−0,03	−0,03	−0,04	−0,02
Sweet Potato	0,81	**0,83**	**0,83**	0,77	0,80	0,81	0,77	**0,83**
Tomato	0,88	0,86	0,86	0,81	**0,90**	0,88	**0,91**	0,83
Wheat	0,70	**0,74**	**0,74**	0,70	0,69	0,70	0,68	0,71

and surface characteristics, and thus, the NDVI exhibits different sensitivity on the evolution of vegetation and its own limitations. It tends to saturate in scenes with a large amount of vegetation, for which it is not sensitive to small changes, and, instead, it is sensitive to the ground when there is low vegetation cover (Huete, 1988). Another clear issue is the limited availability of data due to the presence of clouds, as observed in Section 3.3. Consequently, the correlations obtained for coherence and backscatter ratio with respect to the NDVI need to be properly interpreted and are limited to the data available in the study case. The interpretation is based on using the NDVI as a direct vegetation descriptor, but the applicability of coherence as a vegetation index would need to be further studied by comparing coherence with actual physical descriptors of the crop, like LAI, biomass, or any other relevant physical feature. Regarding the data availability, additional analyses over other years would help confirm the current observations and, in case of less cloud coverage, fix the potential loss of correlation due to missing data.

A key aspect that has been pointed out in this work is that coherence values measured at both VV and VH channels are well correlated to NDVI ($R^2 > 0.7$) for most crop types, and which one is best depends on the crop properties. The VV channel has proved to better describe the development of most crops, although the VH channel is comparably or better correlated for less dense crops. Therefore, the dual-pol operation of Sentinel-1 is an important asset to exploit coherence as a vegetation index, since the performance of one channel or another depends on the crop type.

In addition, we have found that the difference between the coherence measured at the two channels is also correlated to NDVI, but in a clearly lower degree than the channels separately. Consequently, its use is not recommended for crop monitoring.

From a broader point of view, a final purpose of this study was to explore further the potential of using radar data as a tool for agricultural monitoring. Results show that interferometric coherence can, in many cases, emulate the behaviour of the NDVI better than the backscattering time series. Therefore, both information sources (intensity and interferometry) appear to be complementary, as it was demonstrated previously for crop-type mapping (Mestre-Quereda et al., 2020). A notable example is rice, where the changes in the scene properties are better described by backscattering than by coherence. In the literature, the good correlation between SAR and optical time series has been exploited for data fusion, as well as for time series gap filling, i.e., for generating values for the optical sensors whenever they are missing, e.g., due to cloud presence. For instance, some works show the estimation of time series of vegetation parameters (derived initially from optical imagery) by using either SAR backscattered intensity (Mazza et al., 2018) or the RVI (Pipia et al., 2019). In addition, Efremova et al. (2022) combined S1 with S2 images to produce time series of soil moisture estimations by avoiding gaps. In this vein, the interferometric coherence measured with S1 could also be exploited for these purposes, since we found it to be well correlated with NDVI. The performance of this approach is left for a future study.

Attending to the practical usage of S1 coherence for crop monitoring, we have evaluated the necessity to take into account the bias estimation due to finite ENL and the impact of SNR decorrelation. Results have shown that the extra processing steps required to cope with these features are not worth because they have not shown noticeable improvements when trying to correlate the coherence time series with the NDVI curves. Therefore, the coherence directly estimated from the SLC images can be readily exploited. However, it must be noted that the ENL, and hence the estimation window size, must be large enough to ensure the measurable values to be low (below 0.4 and down to 0.2). Otherwise, the dynamic range will be severely affected and coherence would not be sensitive to scene changes along the growing cycle. If the final application is designed to monitor crops at field level, the estimation window can be locally adapted by exploiting the known field boundaries, as it is recommended by Nikaein et al. (2021).

The correlations obtained for different orbits have shown the influence of the observation conditions upon the usage of coherence as a vegetation index. The increase in coherence achieved by some orbits during the initial and final stages of the growing season entails an increased dynamic range, which translates in better correlation with the NDVI and, therefore, a better performance as a vegetation index. It has been seen how an orbit with an acquisition time for a moment of the day with slower winds, as well as a steeper observation, is preferable, with the second factor having the biggest influence.

Finally, the use of a longer temporal baseline (12 days instead of 6 days) resulted in generally worse correlations with NDVI. However, most of the crops still provided high R^2 values (around or above 0.7). This is a key positive aspect because 12 days is the nominal baseline outside Europe, as well as over Europe since the end of 2021 due to the failure of S1-B.

5. Conclusions

The main conclusions of the analysis carried out in this work are summarised in the next bullet points:

- Time series of 6-day repeat-pass coherence from S1 data, measured at both VV and VH channels, can be effectively applied as vegetation indices for agricultural crop monitoring.
- VV coherence is overall the best option at describing the evolution of crops, while VH is better suited for certain less dense crop types (carrot and onion).

- In case more than one orbit is available, the orbit with steepest observation is preferable.
- The processes of bias removal and the separation of sources of decorrelation are not necessary, since they do not provide noticeable improvements when working with VV and VH individually. Therefore, the measured coherence can be directly exploited without any additional processing, provided that the ENL is large enough.
- Interferometric coherence and backscatter (image intensity) provide complementary information as vegetation indices and could be jointly exploited.
- The performance obtained with 12-day temporal baseline is worse than with 6 days but still acceptable for monitoring most of the crops present in the test site.

In this work the performance of coherence as a vegetation index has been evaluated by correlating it with another vegetation index, NDVI. Obviously, the actual contribution of coherence still needs to be studied by comparing it with crop biophysical variables measured in field campaigns. In addition, extending the study to different years and in different geographical locations would help to confirm and fully assess the potential of coherence as a vegetation index for agriculture. Related to this, recent initiatives to generate wide scale (even global) coherence maps with S1 data, as the one conducted by Kellndorfer et al. (2022), would help users to adopt this type of data for new applications, like crop monitoring, for which it has been used much less than backscatter.

CRediT authorship contribution statement

Arturo Villarroya-Carpio: Data curation, Software, Investigation, Visualization, Writing – original draft. **Juan M. Lopez-Sanchez:** Conceptualization, Methodology, Supervision, Writing – original draft. **Marcus E. Engdahl:** Writing – review & editing.

Declaration of competing interest

The authors declare that they have no known competing financial interests or personal relationships that could have appeared to influence the work reported in this paper.

Data availability

The authors do not have permission to share data.

Acknowledgements

This work was supported in part by the European Space Agency under Project SEOM-S14SCI-Land (SInCohMap), and in part by the Spanish Ministry of Science and Innovation (State Agency of Research, AEI) and the European Funds for Regional Development under Project PID2020-117303GB-C22. The reference data were kindly provided by the Regional Government of Andalucía.

References

Bamler, R., Hartl, P., 1998. Synthetic aperture radar interferometry. Inverse Problems 14, R1–54. http://dx.doi.org/10.1088/0266-5611/14/4/001.

Bannari, A., Morin, D., Bonn, F., Huete, A.R., 1995. A rev. vegetation indices. Remote Sens. Rev. 13 (1–2), 95–120. http://dx.doi.org/10.1080/02757259509532298.

Bhogapurapu, N., Dey, S., Bhattacharya, A., Mandal, D., Lopez-Sanchez, J.M., McNairn, H., López-Martínez, C., Rao, Y., 2021. Dual-polarimetric descriptors from sentinel-1 GRD SAR data for crop growth assessment. ISPRS J. Photogramm. Remote Sens. 178, 20–35. http://dx.doi.org/10.1016/j.isprsjprs.2021.05.013.

Bhogapurapu, N., Dey, S., Mandal, D., Bhattacharya, A., Karthikeyan, L., McNairn, H., Rao, Y., 2022. Soil moisture retrieval over croplands using dual-pol L-band GRD SAR data. Remote Sens. Environ. 271, http://dx.doi.org/10.1016/j.rse.2022.112900.

Blaes, X., Defourny, P., 2003. Retrieving crop parameters based on tandem ERS 1/2 interferometric coherence images. Remote Sens. Environ. 88 (4), 374–385. http://dx.doi.org/10.1016/j.rse.2003.08.008.

Busquier, M., Lopez-Sanchez, J.M., Mestre-Quereda, A., Navarro, E., González-Dugo, M.P., Mateos, L., 2020. Exploring TanDEM-X interferometric products for crop-type mapping. Remote Sens. 12 (11), http://dx.doi.org/10.3390/rs12111774.

Di Martino, T., Guinvarch, R., Thirion-Lefevre, L., Koeniguer, E., 2022. Beets or cotton? Blind extraction of fine agricultural classes using a convolutional autoencoder applied to temporal SAR signatures. IEEE Trans. Geosci. Remote Sens. 60, http://dx.doi.org/10.1109/TGRS.2021.3100637.

Efremova, N., Seddik, M.E.A., Erten, E., 2022. Soil moisture estimation using sentinel-1/-2 imagery coupled with CycleGAN for time-series gap filing. IEEE Trans. Geosci. Remote Sens. 60, 1–11. http://dx.doi.org/10.1109/TGRS.2021.3134127.

Engdahl, M., Borgeaud, M., Rast, M., 2001. The use of ERS-1/2 tandem interferometric coherence in the estimation of agricultural crop heights. IEEE Trans. Geosci. Remote Sens. 39 (8), 1799–1806. http://dx.doi.org/10.1109/36.942558.

Engdahl, M., Hyyppä, J., 2003. Land-cover classification using multitemporal ERS-1/2 InSAR data. IEEE Trans. Geosci. Remote Sens. 41 (7), 1620–1628. http://dx.doi.org/10.1109/TGRS.2003.813271.

Erten, E., Lopez-Sanchez, J.M., Yuzugullu, O., Hajnsek, I., 2016. Retrieval of agricultural crop height from space: A comparison of SAR techniques. Remote Sens. Environ. 187, 130–144. http://dx.doi.org/10.1016/j.rse.2016.10.007.

Haboudane, D., Miller, J.R., Pattey, E., Zarco-Tejada, P.J., Strachan, I.B., 2004. Hyperspectral vegetation indices and novel algorithms for predicting green LAI of crop canopies: Modeling and validation in the context of precision agriculture. Remote Sens. Environ. 90 (3), 337–352. http://dx.doi.org/10.1016/j.rse.2003.12.013.

Huete, A., 1988. A soil-adjusted vegetation index (SAVI). Remote Sens. Environ. 25 (3), 295–309. http://dx.doi.org/10.1016/0034-4257(88)90106-X.

Jacob, A.W., et al., 2020. Sentinel-1 InSAR coherence for land cover mapping: A comparison of multiple feature-based classifiers. IEEE J. Sel. Top. Appl. Earth Obs. Remote Sens. 13, 535–552. http://dx.doi.org/10.1109/JSTARS.2019.2958847.

Kellndorfer, J., Cartus, O., Lavalle, M., Magnard, C., Milillo, P., Oveisgharan, S., Osmanoglu, B., Rosen, P.A., Wegmuller, U., 2022. Global seasonal Sentinel-1 interferometric coherence and backscatter data set. Sci. Data 9, http://dx.doi.org/10.1038/s41597-022-01189-6.

Khabbazan, S., Vermunt, P., Steele-Dunne, S., Ratering Arntz, L., Marinetti, C., van der Valk, D., Iannini, L., Molijn, R., Westerdijk, K., van der Sande, C., 2019. Crop monitoring using Sentinel-1 data: A case study from The Netherlands. Remote Sens. 11 (16), http://dx.doi.org/10.3390/rs11161887.

Kim, Y., van Zyl, J.J., 2009. A time-series approach to estimate soil moisture using polarimetric radar data. IEEE Trans. Geosci. Remote Sens. 47 (8), 2519–2527. http://dx.doi.org/10.1109/TGRS.2009.2014944.

Lee, J.-S., Pottier, E., 2009. Polarimetric Radar Imaging: From Basics to Applications. CRC Press, http://dx.doi.org/10.1201/9781420054989.

Lee, S.-K., Yoon, S.Y., Won, J.-S., 2018. Vegetation height estimate in rice fields using single polarization TanDEM-X science phase data. Remote Sens. 10 (11), http://dx.doi.org/10.3390/rs10111702.

Lopez-Sanchez, J.M., Vicente-Guijalba, F., Erten, E., Campos-Taberner, M., Garcia-Haro, F.J., 2017. Retrieval of vegetation height in rice fields using polarimetric SAR interferometry with TanDEM-X data. Remote Sens. Environ. 192, 30–44. http://dx.doi.org/10.1016/j.rse.2017.02.004.

Mandal, D., Bhattacharya, A., Rao, Y.S., 2021. Radar Remote Sensing for Crop Biophysical Parameter Estimation. Springer, http://dx.doi.org/10.1007/978-981-16-4424-5.

Mandal, D., Kumar, V., Ratha, D., Dey, S., Bhattacharya, A., Lopez-Sanchez, J.M., McNairn, H., Rao, Y.S., 2020a. Dual polarimetric radar vegetation index for crop growth monitoring using sentinel-1 SAR data. Remote Sens. Environ. 247, 111954. http://dx.doi.org/10.1016/j.rse.2020.111954.

Mandal, D., Ratha, D., Bhattacharya, A., Kumar, V., McNairn, H., Rao, Y.S., Frery, A.C., 2020b. A radar vegetation index for crop monitoring using compact polarimetric SAR data. IEEE Trans. Geosci. Remote Sens. 58 (9), 6321–6335. http://dx.doi.org/10.1109/TGRS.2020.2976661.

Mazza, A., Gargiulo, M., Scarpa, G., Gaetano, R., 2018. Estimating the NDVI from SAR by convolutional neural networks. In: IGARSS 2018 - 2018 IEEE International Geoscience and Remote Sensing Symposium. pp. 1954–1957. http://dx.doi.org/10.1109/IGARSS.2018.8519459.

Mestre-Quereda, A., Lopez-Sanchez, J.M., Vicente-Guijalba, F., Jacob, A.W., Engdahl, M.E., 2020. Time-series of Sentinel-1 interferometric coherence and backscatter for crop-type mapping. IEEE J. Sel. Top. Appl. Earth Obs. Remote Sens. 13, 4070–4084. http://dx.doi.org/10.1109/JSTARS.2020.3008096.

Nasirzadehdizaji, R., Cakir, Z., Balik Sanli, F., Abdikan, S., Pepe, A., Calò, F., 2021. Sentinel-1 interferometric coherence and backscattering analysis for crop monitoring. Comput. Electron. Agric. 185, 106118. http://dx.doi.org/10.1016/j.compag.2021.106118.

Nikaein, T., Iannini, L., Molijn, R.A., Lopez-Dekker, P., 2021. On the value of Sentinel-1 InSAR coherence time-series for vegetation classification. Remote Sens. 13 (16), http://dx.doi.org/10.3390/rs13163300.

Palmisano, D., Mattia, F., Balenzano, A., Satalino, G., Pierdicca, N., Guarnieri, A.V.M., 2021. Sentinel-1 sensitivity to soil moisture at high incidence angle and the impact on retrieval over seasonal crops. IEEE Trans. Geosci. Remote Sens. 59 (9), 7308–7321. http://dx.doi.org/10.1109/TGRS.2020.3033887.

Pandit, A., Sawant, S., Mohite, J., Pappula, S., 2022. Sentinel-1-derived coherence time-series for crop monitoring in Indian agriculture region. Geocarto Int. 1–21. http://dx.doi.org/10.1080/10106049.2021.2022008.

Pipia, L., Muñoz-Marí, J., Amin, E., Beld, S., Camps-Valls, G., Verrelst, J., 2019. Fusing optical and SAR time series for LAI gap filling with multioutput Gaussian processes. Remote Sens. Environ. 235, 111452. http://dx.doi.org/10.1016/j.rse.2019.111452.

Potin, P., Gascon, F., Stromme, A., Zehner, C., 2021. Sentinel High Level Operations Plan. Technical Document, ESA, Online URL https://sentinel.esa.int/web/sentinel/missions/sentinel-1/observation-scenario. (Accessed 09 June 2022).

Romero-Puig, N., Lopez-Sanchez, J.M., 2021. A review of crop height retrieval using InSAR strategies: Techniques and challenges. IEEE J. Sel. Top. Appl. Earth Obs. Remote Sens. 14, 7911–7930. http://dx.doi.org/10.1109/JSTARS.2021.3100874.

Rosen, P., Hensley, S., Joughin, I., Li, F., Madsen, S., Rodriguez, E., Goldstein, R., 2000. Synthetic aperture radar interferometry. Proc. IEEE 88 (3), 333–382. http://dx.doi.org/10.1109/5.838084.

SIAR, 2022. Sistema de Información Agroclimática para el Regado. Gobierno de España. Ministerio de Agricultura, Pesca y Alimentación. Online https://eportal.mapa.gob.es/websiar/Inicio.aspx. (Accessed 09 June2022).

Sica, F., Pulella, A., Nannini, M., Pinheiro, M., Rizzoli, P., 2019. Repeat-pass SAR interferometry for land cover classification: A methodology using Sentinel-1 short-time-series. Remote Sens. Environ. 232, 111277. http://dx.doi.org/10.1016/j.rse.2019.111277.

Steele-Dunne, S.C., McNairn, H., Monsivais-Huertero, A., Judge, J., Liu, P.-W., Papathanassiou, K., 2017. Radar remote sensing of agricultural canopies: A review. IEEE J. Sel. Top. Appl. Earth Obs. Remote Sens. 10 (5), 2249–2273. http://dx.doi.org/10.1109/JSTARS.2016.2639043.

Strozzi, T., Dammert, P., Wegmuller, U., Martinez, J.-M., Askne, J., Beaudoin, A., Hallikainen, N., 2000. Landuse mapping with ERS SAR interferometry. IEEE Trans. Geosci. Remote Sens. 38 (2), 766–775. http://dx.doi.org/10.1109/36.842005.

Touzi, R., Lopes, A., Bruniquel, J., Vachon, P., 1999. Coherence estimation for SAR imagery. IEEE Trans. Geosci. Remote Sens. 37 (1), 135–149. http://dx.doi.org/10.1109/36.739146.

Vincent, P., Bourbigot, M., Johnsen, H., Piantanida, R., 2017. Thermal Denoising of Products Generated by the S-1 IPF. REFERENCE: MPC - 0392. Technical Document, ESA, Online URL https://sentinel.esa.int/web/sentinel/user-guides/document-library. (Accessed 09 June 2022).

Wegmuller, U., Werner, C., 1997. Retrieval of vegetation parameters with SAR interferometry. IEEE Trans. Geosci. Remote Sens. 35 (1), 18–24. http://dx.doi.org/10.1109/36.551930.

Zebker, H., Villasenor, J., 1992. Decorrelation in interferometric radar echoes. IEEE Trans. Geosci. Remote Sens. 30 (5), 950–959. http://dx.doi.org/10.1109/36.175330.